polymers

IMPACT FACTOR 4.9

Indexed in: PubMed

CITESCORE 9.7

Article

Biological and Biophysical Characterization of Hybrid PLCL Nanofibers Incorporating Stem Cell-Derived Secretome

Tanya Stoyanova, Lora Topalova, Dencho Gugutkov, Regina Komsa-Penkova, Stanimir Kyurkchiev, Iren Bogeva-Tsolova, Dobromir Dimitrov, Svetla Todinova and George Altankov

MDPI

https://doi.org/10.3390/polym18040528

polymers

MDPI

Article

Biological and Biophysical Characterization of Hybrid PLCL Nanofibers Incorporating Stem Cell-Derived Secretome

Tanya Stoyanova [1,2,†], Lora Topalova [1,2,†], Dencho Gugutkov [2], Regina Komsa-Penkova [2,3], Stanimir Kyurkchiev [4], Iren Bogeva-Tsolova [2,5], Dobromir Dimitrov [6], Svetla Todinova [1] and George Altankov [2,7,8,*]

1 Institute of Biophysics and Biomedical Engineering, Bulgarian Academy of Sciences, 1113 Sofia, Bulgaria; tanya.zh.stoyanova@gmail.com (T.S.); topalovaloram@gmail.com (L.T.); todinova@abv.bg (S.T.)
2 Center of Competence in Personalized Medicine, 3D and Telemedicine, Robotic Assisted and Minimally Invasive Surgery-"Leonardo da Vinci", 5800 Pleven, Bulgaria; denchog@abv.bg (D.G.); regina.komsa-penkova@mu-pleven.bg (R.K.-P.); irenbogeva@outlook.com (I.B.-T.)
3 Department of Biochemistry, Medical University-Pleven, 5800 Pleven, Bulgaria
4 Tissue Bank BulGen, 1330 Sofia, Bulgaria; stanimirkyurkchiev@gmail.com
5 Department of Surgery, Faculty of Medicine, Medical University-Pleven, 5800 Pleven, Bulgaria
6 Department of Surgical Propaedeutics, Medical University-Pleven, 5800 Pleven, Bulgaria; dobri_dimitrov@abv.bg
7 Associate Project BG-RRP-2.004-0003, Medical University-Pleven, 5800 Pleven, Bulgaria
8 Research Institute, Medical University-Pleven, 5800 Pleven, Bulgaria
* Correspondence: altankov@abv.bg
† These authors contributed equally to this work.

Abstract

The design of multifunctional biomaterials that offer both structural support and biochemical cues is essential for enhancing tissue regeneration. In this study, hybrid nanofibrous scaffolds composed of poly(L-lactide-co-ε-caprolactone) (PLCL) and bioactive factors secreted by Wharton's jelly-derived mesenchymal stem cells (WJ-MSCs) were fabricated via co-electrospinning. Nanofibers were produced in aligned and random configurations following an optimized protocol developed at the Institute for Bioengineering of Catalonia (IBEC). Their morphology and topography were characterized by light microscopy, scanning electron microscopy (SEM), and atomic force microscopy (AFM), and fiber orientation was quantified via Fast Fourier Transform (FFT) analysis. The scaffolds showed fiber diameters of 542.9 ± 62.3 nm, with aligned fibers predominantly oriented within 20° of the principal axis. Human AD-MSCs were used to assess biocompatibility and cell–material interactions. Aligned and random nanofiber architectures elicited distinct cellular responses. AD-MSCs on aligned fibers exhibited smaller spreading areas (~320 μm^2) vs. on random nanofibers (~500 μm^2) and substantially higher proliferation, resulting in a shorter cell-doubling time (~25 h) than those on random nanofibers (~130 h) or control substrates (~70 h). In addition, aligned nanofibers promoted markedly faster migration, reaching rates of ~5000 μm^2/h surface coverage, compared with random nanofibers (~770 μm^2/h) and controls (~1800 μm^2/h). Together, the results show that nanofiber alignment and biochemical functionalization jointly influence MSC behavior and improve regeneration, highlighting the potential of these PLCL-based hybrid secretome/PLCL nanofibers for advanced wound healing.

Keywords: hybrid secretome/PLCL nanofibers; electrospinning; mesenchymal stem cells; Wharton's jelly stem cells secretome; wound healing; tissue regeneration

Academic Editor: Gang Wei

Received: 3 February 2026
Revised: 17 February 2026
Accepted: 18 February 2026
Published: 21 February 2026

1. Introduction

Chronic, non-healing wounds remain a critical clinical problem and a major burden on healthcare systems worldwide. Conditions such as diabetic ulcers, burns, pressure injuries, and venous leg ulcers are associated with impaired tissue repair, recurrent infections, and prolonged treatment period, affecting millions of patients and generating substantial morbidity and healthcare costs [1]. Conventional wound care approaches, comprising various dressings, topical agents, and surgical interventions, are often insufficient because they primarily offer physical protection without providing biomimetic stimuli required for effective tissue regeneration [2]. Consequently, there is an urgent need to develop bioengineered materials that actively modulate the wound microenvironment to accelerate repair and restore tissue functionality [3].

Tissue engineering offers various promising strategies to recreate the structure and function of native tissues. Among them, nanofibers fabrication techniques, such as electrospinning, have emerged as a versatile approach to produce nanofibrous scaffolds that closely mimic the extracellular matrix (ECM) architecture [4]. Moreover, nanofibers exhibit a high surface-to-volume ratio, tunable porosity and orientation, and mechanical flexibility, all of which strongly influence cellular interaction [5].

A variety of materials have been explored for wound-healing applications, including natural polymers such as collagen, chitosan, alginate, and silk fibroin, as well as synthetic polymers like poly(ε-caprolactone) (PCL), poly(lactic acid) (PLA), and polyurethane [6–8]. These materials differ in their mechanical properties, degradation profiles, and bioactivity, and they are often modified or combined to enhance their performance. Recent engineering-focused analyses have further emphasized the importance of structure–property optimization in fibrous materials, reinforcing the relevance of design–performance correlations in scaffold development [9]. In this respect, poly(L-lactide-co-ε-caprolactone) (PLCL) has garnered considerable attention as a biodegradable and biocompatible copolymer [10], making it highly suitable for a wide range of biomedical applications [11]. Its unique composition combines the relative rigidity of PLA with the elasticity of PCL, enabling the fabrication of scaffolds that closely mimic the mechanical properties of soft tissues [12,13].

However, despite its favorable mechanical characteristics and biodegradability, synthetic PLCL remains inherently bioinert and therefore requires functionalization with bioactive compounds [10,14,15]. Numerous studies have demonstrated that the biological performance of PLCL scaffolds can be significantly enhanced through surface modification or bulk incorporation of bioactive cues, including proteins, peptides, and extracellular vesicle-derived factors [6,8,16,17]. In this respect electrospinning, except providing a highly adaptable fabrication platform that enables precise control over fiber diameter, alignment, and porosity, while also allowing quantitative incorporation of bioactive molecules directly into the nanofiber matrix [7,18–20]. Such biomimetic functionalization has been shown to influence cell adhesion, proliferation, and differentiation in a predictable manner, establishing a clear relationship between processing parameters, scaffold architecture, and biological function [21–23].

In parallel, mesenchymal stem cells (MSCs) play a central role in biomaterial-based regenerative therapies due to their multipotent ability to self-renew and differentiate into various mesodermal lineages. Originally isolated from bone marrow, MSCs have since been identified in multiple anatomical sources, including adipose tissue, placenta, tooth pulp, and the umbilical cord [24]. While their differentiation capacity was initially considered the primary mechanism of action, current evidence underscores the importance of their paracrine signaling as the dominant contributor to tissue repair [25].

The MSC secretome, collected from conditioned culture medium, contains a diverse repertoire of soluble bioactive molecules and extracellular vesicles and has been shown

to play a pivotal role in orchestrating regenerative processes. These include angiogenic factors such as vascular endothelial growth factor (VEGF) and basic fibroblast growth factor (bFGF), which stimulate neovascularization; proliferative and migratory cues like epidermal growth factor (EGF) and hepatocyte growth factor (HGF); and immunomodulatory agents such as transforming growth factor-β (TGF-β) and interleukin-10 (IL-10), which regulate inflammation and immune responses [26]. In addition, the secretome contains extracellular matrix (ECM) proteins and adhesive molecules (like fibronectin, laminin fragments, etc.) [27] that support cellular attachment, as well as antimicrobial peptides such as LL-37 and β-defensins [28,29], which contribute to infection control. In addition, various messenger RNAs (mRNAs) have proven pivotal in intracellular communication. Several studies have demonstrated its successful application in tissue engineering, where MSC-derived conditioned media or extracellular vesicles have been incorporated into biomaterials such as hydrogels to enhance wound healing, bone regeneration, and cartilage repair [30,31]. These approaches highlight the translational potential of the MSC secretome, offering advantages such as reduced immunogenicity, avoidance of cell survival issues, and easier storage and handling compared to live cell therapies [8,32]. Therefore, integrating the biomimetic properties of PLCL nanofibers with the characteristic bioactivity of the MSC secretome could yield an ideal wound dressing material (or regenerative patch)—capable of delivering bioactive factors in a sustained manner while serving as a substrate that guides the directional migration of autologous stem cells toward the site of injury.

Our recent study [33] demonstrated that the secretome derived from Wharton's Jelly mesenchymal stem cells (WJ-MSCs) selectively enhances the functional activity of adipose-derived MSCs (AD-MSCs), while preserving the quiescent state of dermal fibroblasts. This targeted paracrine modulation highlights the sophisticated regulatory capacity of the WJ-MSC secretome and supports its potential for the development of precision regenerative therapies. We propose that incorporating WJ-MSC-derived bioactive molecules into electrospun nanofibrous scaffolds will generate a construct with broad and complementary functionalities. In this design, (i) the PLCL matrix provides mechanical support that closely resembles the properties of native soft tissues, (ii) the nanofibrous architecture offers a flexible platform for the spatial presentation of both adhesive cues and soluble bioactive factors, and (iii) the composite scaffold creates a finely regulated microenvironment capable of controlled paracrine factor release, thereby enhancing tissue regeneration. Such integrated strategy addresses key limitations of conventional biomaterial-based therapies and is consistent with emerging principles in bioresponsive wound-care engineering.

More specifically, this study aims to engineer bioactive hybrid PLCL nanofibers incorporating secretome-derived molecules from umbilical cord MSCs via electrospinning. The resulting scaffold was characterized with respect to its morphology, release kinetics, and in vitro biological activity, using AD-MSCs from an independent donor as a cellular model to assess adhesion, proliferation, and directional migration, as well as to determine how fiber alignment modulates their functional behavior.

2. Materials and Methods

2.1. Secretome Preparation

The procedure for secretome preparation followed a previously established protocol [33] and was provided by Tissue Bank BulGen (Sofia, Bulgaria). Briefly, human umbilical cord tissue from healthy donors was obtained with informed consent, approved by the Ethics Committee of Ob/Gyn Hospital Dr. Shterev, Sofia, Bulgaria. Mesenchymal stem cells (MSCs) were isolated and characterized based on the expression of MSC-specific markers and absence of hematopoietic ones. Umbilical cord segments (2.5 cm) were dissected to remove blood vessels, minced, and enzymatically digested with 0.25% Collagenase I,

4 mg/mL hyaluronidase, and 1% antibiotic-antimycotic solution (all from Sigma-Aldrich, St. Louis, MO, USA) at 37 °C for 3 h in a humidified 5% CO_2 incubator. The digested tissue was filtered through a 70 µm strainer and centrifuged at 876× *g* for 10 min. The cell pellet was re-suspended in DMEM/F12, supplemented with 10% FBS and 1% antibiotic-antimycotic solution (all from Sigma-Aldrich), then seeded at density 1 × 10^4 cells per 25 cm^2 flask. Medium was refreshed every 48 h until cells reached around 80–90% density. At that point, the medium was replaced with fresh 5 mL serum-free medium and cultured for 48 h before being collected. The collected medium containing secretome was centrifuged at 876× *g* for 10 min (to remove debris) and concentrated 10 times using Amicon Ultra centrifugal filter units (Amicon, Schorndorf, Germany). The protein concentration was measured using Bradford assay (Sigma-Aldrich, USA) and determined to be approx. 0.3 mg/mL. The secretome was then lyophilized and stored at −80 °C until use.

2.2. Electrospining

Poly(L-lactide-co-ε-caprolactone) (PLCL) (Sigma-Aldrich, USA) used for the electrospinning was ester-terminated with a feed ratio of lactide:caprolactone 70:30. PLCL was dissolved in hexafluoroisopropanol (HFIP) (Sigma-Aldrich, USA) at 120 mg/mL at room temperature. Ready-to-use, lyophilized Wharton's jelly mesenchymal stem cells (WJ-MSCs) secretome was provided by Tissue Bank BulGen (Sofia, Bulgaria) and dissolved in HFIP at 0.6 mg/mL. The PLCL solution and WJ-MSCs secretome solution were mixed in equal volumes (1 mL each; 1:1 *v*/*v*) prior to electrospinning (Figure 1), yielding a final concentration of 6% (*w*/*v*) PLCL with 0.3 mg/mL secretome content. The choice of this ratio was based on a series of preliminary optimization experiments aimed at ensuring consistent nanofiber production and maintaining batch-to-batch reproducibility. Nanofibers were fabricated using the Spinbox electrospinning device (Bioinicia Fluidnatek SLU, Valencia, Spain) equipped with a 10 cm in diameter rotating drum. The system utilizes a single-needle (outer diameter: 1.27 mm) electrospinning setup equipped with an auxiliary needle electrode connected to the 5 mL syringe (inner diameter: 12.55 mm, Chirana, Stara Tura, Slovakia). Randomly deposited hybrid secretome PLCL nanofibers (R-SNFs) were obtained by electrospining the polymer–secretome solution for 10 min onto regular glass coverslips (12 × 12 mm, ISOLAB Laborgeräte GmbH, Eschau, Germany) placed on the grounded Spinbox plate, at a distance of 14 cm. The aligned hybrid secretome PLCL nanofibers (A-SNFs) were obtained onto the rotating drum, at the same distance of 14 cm. The applied voltage was 10 kV and the flow rate was 1.5 µL/min for synthesizing R-SNFs and 4 µL/min for A-SNFs. Electrospinning was performed under ambient laboratory conditions (approximately 20 °C and ~60% relative humidity). The fibers were collected following the protocol originally developed at the Institute for Bioengineering of Catalonia (IBEC) Barcelona, Spain [34]. As a control, plain PLCL nanofibers (CNFs) were electrospun from a 12% (*w*/*v*) solution under the same conditions in both random and aligned configurations. A 12% PLCL concentration was selected as the minimal polymer content that consistently produced stable, uniform fibers in our optimization experiments, as lower concentrations led to jet instability, bead formation, and electrospraying.

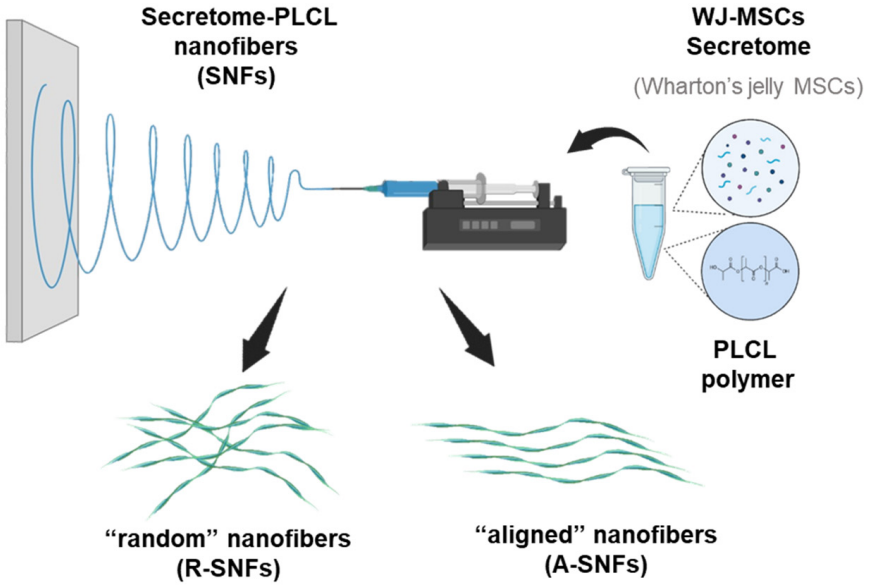

Figure 1. Schematic illustration of the electrospinning setup and formation of hybrid secretome PLCL nanofibers. The electrospinning mixture is composed from Wharton's jelly secretome and PLCL polymer, then the secretome nanofibers (SNFs) were electrospun in two configurations—random (R-SNFs) and aligned (A-SNFs).

2.3. Fast Fourier Transformation (FFT) Analysis with ImageJ

The nanofibers were observed under a phase-contrast microscope (Leica DM 2900, Leica Microsystems, Heerbrugg, Switzerland) at 20× magnification, and then typical images were obtained. The images were further analyzed using ImageJ software version 1.54p (Wayne Rasband, National Institute of Mental Health, NIH, Bethesda, MD, USA) where Fast Fourier Transformation (FFT) tool was applied to characterize the alignment of the fibers. The frequency distribution from the FFT output was visualized by overlaying a circular projection using the Oval Profile plug-in in ImageJ [35]. This process involved measuring the radial sum of pixel intensities at 1° intervals from 0° to 180°. All FFT data were normalized to a baseline and expressed in arbitrary units to enable direct comparison across datasets.

The same FFT analysis was also applied to analyze the alignment of the adhering stem cells. For this purpose, AD-MSCs were seeded at a concentration of 3×10^4 cells per well in a 6-well plate, containing aligned and random SNFs deposited on regular 12 × 12 mm glass coverslips and cultured under standard conditions (as detailed below) for 24 h. Cells seeded on glass coverslips without nanofibers were used as a control. Live cells were visualized by incubating the samples with 2 µM Calcein AM (Thermo Fisher Scientific Waltham, MA, USA) in DMEM/F12 culture medium (Sigma-Aldrich, USA) supplemented with 1% antibiotic-antimycotic solution (Sigma-Aldrich, USA) for 30 min at 37 °C, allowing viable cells to be selectively stained with bright green fluorescence. After staining, fluorescent images were captured using a fluorescence microscope Thunder Imager Live Cell (Leica Microsystems, Heerbrugg, Switzerland) under standardized exposure settings. These images further underwent the same FFT processing pipeline as that for the nanofibers to evaluate the overall orientation and alignment of the cells relative to the substrate.

2.4. FITC Labeling of WJ-MSCs' Bioactive Molecules and Purification by Gel Permeation Chromatography (GPC)

Fluorescein isothiocyanate (FITC) labeling followed by Gel Permeation Chromatography (GPC) was performed to generate a fluorescently tagged secretome, enabling verification of its successful incorporation into the PLCL nanofibers and its subsequent release

into the medium. Briefly, the lyophilized WJ-MSC secretome was dissolved in 1 mL carbonate–bicarbonate buffer (pH ≈ 9) (Sigma-Aldrich, USA) to a final protein concentration of 0.6 mg/mL. Subsequently, 7 µL of a 10 mg/mL FITC stock solution (Sigma-Aldrich, USA) was added to achieve a final concentration of 70 µg/mL. The mixture was incubated for 1 h at room temperature in the dark. Excess FITC was removed by Gel Permeation Chromatography using a PD-10 Sephadex G-25M size-exclusion column (Cytiva, Marlborough, MA, USA) equilibrated with PBS. The sample was eluted with a Lambda Preciflow pump (LAMBDA Laboratory Instruments, Brno, Czech Republic) at a constant flow rate of 1 mL/min. Eluted solution was monitored using a Spectra/Chrom UV Monitor Model 280 (Spectrum Labs, San Francisco, CA, USA) at 280 nm. Fractions corresponding to FITC-labeled proteins with maximum adsorption at 280 nm and 495 nm were collected, pooled, and stored at 4 °C in the dark until use. Fluorescent imaging of nanofibers was made using an inverted fluorescent microscope Thunder Imager Live Cell (Leica Microsystems, Heerbrugg, Switzerland).

2.5. Protein Release Assay

FITC-protein release from the SNFs was assessed by incubating the samples in 2 mL phosphate-buffered saline (PBS, pH 7.4) (Sigma-Aldrich, USA) containing 0.01% NaN_3 at 37 °C for 7 days. As a control for non-specific fluorescence, CNFs and non-labeled SNFs were used. The mass of each sample was approximately 20 mg (equal to about 0.1 mg protein for SNFs samples). The released FITC-labeled protein was quantified by measuring the fluorescence intensity (excitation 495 nm/emission 519 nm) using a spectrofluorometer (FP-8050, Jasco Inc., Mary's Court Easton, MD, USA).

2.6. Fourier Transform Infrared (FTIR) Spectroscopy

Fourier Transform infrared (FTIR) spectroscopy was performed to identify the characteristic functional groups of the control PLCL nanofibers (CNFs) and to evaluate potential chemical changes resulting from the fabrication process and from the inclusion of secretome products. Spectra were collected using a Nicolet™ iS5 FTIR spectrophotometer (Thermo Fisher Scientific, USA) equipped with an iD5 attenuated total reflectance (ATR) accessory. Prior to analysis, nanofiber mats were cut into small pieces and placed directly onto the ATR crystal to ensure uniform contact. Spectra were recorded in the range of 4000–550 cm^{-1} with a spectral resolution of 4 cm^{-1}, averaging at 32 scans per sample to improve the signal-to-noise ratio. Background spectra were collected before each measurement and automatically subtracted from the sample. All spectra were processed using the instrument's proprietary software, applying baseline correction and normalization where appropriate. Spectral processing and peak analysis were performed using Spectragryph 1.2.16.1 (Dr. Friedrich Menges Software Entwicklung, Oberstdorf, Germany).

2.7. Scanning Electron Microscopy (SEM) and Nonofiber Diameter Distribution Analysis

SEM images of random and aligned samples were acquired using Phenom Pro G6 Desktop SEM. Histograms of the diameter distribution of the nanofibers were obtained using ImageJ, software version 1.54p (Wayne Rasband, National Institute of Mental Health, NIH, Bethesda, MD, USA).

2.8. Atomic Force Microscopy (AFM)

Random and aligned PLCL nanofibers were characterized using AFM to obtain high-resolution topographical images and quantitative surface parameters. The measurements were generously performed at the Laboratory of Park Systems UK using a Park Systems NX12 atomic force microscope (Park Systems, Nottingham, UK).

Topography measurements were carried out in non-contact mode (NCM), and for nanomechanical measurements in PinPoint mode. This approach enables simultaneous acquisition of high-resolution topographical images and point-resolved mechanical information obtaining force–distance curves at each pixel of the entire scan area while minimizing lateral shear forces, which is particularly advantageous for polymeric nanofibers.

Large-area images (50 μm × 50 μm) were first acquired in NCM to identify representative fibers. Individual fibers were then selected, and the scan area was zoomed so that PinPoint™ nanomechanical measurements could be performed directly on top of the fibers.

In PinPoint™ mode, a complete force–distance curve was acquired at each pixel of the predefined scan area. During each measurement cycle, the cantilever approached the sample surface vertically until a set maximum force was reached, followed by retraction. This pixel-by-pixel force spectroscopy allowed site-specific quantitative assessment of nanomechanical properties without continuous tip-sample contact. Force-distance curves were analyzed automatically using Park Systems' SmartScan™ software (current release as of 2025).

The Young's modulus (Ea) was calculated from the approach segment of the force–distance curves using the Derjaguin-Muller-Toporov (DMT) contact mechanics model, which is considered appropriate for materials exhibiting relatively low adhesion forces and small indentation depths, such as polymeric nanofibers. For each sample, modulus values were averaged over multiple regions of interest to ensure statistical robustness.

2.9. Cell Culturing

Human adipose tissue derived mesenchymal stem cells (AD-MSCs) used for the experiments were obtained by Tissue Bank BulGen (Sofia, Bulgaria) with informed consent from donors prior to liposuction. Cells were cultured in DMEM/F12 medium supplemented with 10% fetal bovine serum (FBS) (both from Sigma-Aldrich, USA) and 1% antibiotic-antimycotic solution (Sigma-Aldrich, USA) in a humidified thermostat at 37 °C, 5% CO_2. The medium was replaced every 2 to 3 days until cells reached ~90% confluence and then passaged using 0.05% trypsin/0.6 mM EDTA (Sigma-Aldrich, USA). Cells used for experiments were between passages 4 and 6.

2.10. Live–Dead Analysis

AD-MSCs were seeded at a concentration of 3×10^4 cells per well in a 6-well plate onto aligned and random SNFs deposited on regular glass 12 × 12 mm coverslips as above, which were previously sterilized with 70% ethanol (Sigma-Aldrich, USA) followed by complete evaporation under sterile conditions. This approach provides effective antimicrobial action while preserving fiber structure and minimizes the likelihood of significant compositional changes. The seeded samples were cultured in 2 mL DMEM/F12, supplemented with 10% FBS and 1% antibiotic-antimycotic solution (all from Sigma-Aldrich, USA) under standard conditions (37 °C, 5% CO_2) for 24, 48, and 72 h. To evaluate cell viability at each time point, live and dead cells were simultaneously stained using Cellstain Double Staining Kit (Sigma-Aldrich, Cat. No. 04511) according to the manufacturer's instructions. Briefly, the staining solution was prepared fresh and applied to each sample, followed by incubation at 37 °C for 15 min in the dark. Fluorescent images were then acquired using a fluorescence microscope Thunder Imager Live Cell (Leica Microsystems, Heerbrugg, Switzerland) with appropriate filter sets to differentiate live (green fluorescence) and dead (red fluorescence) cells.

2.11. Cell Adhesion and Overall Morphology

AD-MSCs were seeded onto the pre-sterilized (as explained in Section 2.10.) control PLCL nanofibers and SNFs loaded on regular glass coverslips (12 × 12 mm, ISOLAB

Laborgeräte GmbH, Eschau, Germany) at density of 3×10^4 cells/cm^2 and cultured in a 35 mm Petri dish—with 2 mL serum-free medium DMEM/F12, at 37 °C, in a humidified incubator with 5% CO_2—for 2 h to allow cell attachment. After that, 10% FBS (Sigma-Aldrich, USA) was added and the sample was further cultured for 3 h. Cell attachment was initially observed under phase-contrast microscope and then fixed with 4% paraformaldehyde (Sigma-Aldrich, USA) for 10 min at room temperature. After that, the cells were permeabilized with 0.5% Triton X-100 (Sigma-Aldrich, USA) for 5 min and stained with FITC-Phaloidin (Invitrogen, Thermo Fisher Scientific, USA) (dilution 1:100) for 30 min to visualize actin cytoskeleton. The nuclei were counterstained with Hoechst 33258 (1:2000) (Sigma-Aldrich, USA) before being washed and mounted with Mowiol (Polysciences, Inc., Warrington, PA, USA). Representative pictures of the adhered cells were then taken using fluorescent microscope Thunder Imager Live Cell (Leica Microsystems, Heerbrugg, Switzerland) and the corresponding software. In order to determine the overall cell shape, the CellProfiler software version 4.2.8 [36] was used.

2.12. Cell Proliferation Assay

AD-MSCs were seeded at a concentration of 3×10^4 cells per well in a 6-well plate onto aligned and random SNFs deposited on glass coverslips and pre-sterilized (as explained in Section 2.10). The cells were then cultured in 2 mL DMEM/F12 (Sigma-Aldrich, USA) supplemented with 1% antibiotic-antimycotic solution (Sigma-Aldrich, USA) under standard conditions (37 °C, 5% CO_2) in the 6-well plates. To assess cell proliferation, samples were analyzed at 24, 48, and 72 h of culture. At each time point, cells were fixed with 4% paraformaldehyde (Sigma-Aldrich, USA) and subsequently stained with Hoechst 33258 (1:2000 dilution, Sigma-Aldrich, USA) to visualize cell nuclei. Fluorescence images were acquired using a fluorescence microscope Thunder Imager Live Cell (Leica Microsystems, Heerbrugg, Switzerland) with a 10× objective. Quantification of cell number was performed using CellProfiler software to enable objective and reproducible counting of nuclei. The doubling time was calculated by using the following formula:

$$\text{Doubling Time} = [T \times (\ln 2)]/[\ln(N_e/N_b)],$$

where N_b is the initial cell density, N_e is the final cell density and T is the time passed between the two measurements.

2.13. Visualization of Focal Adhesions

The cells were seeded as described above. To visualize focal adhesions, fixed and permeabilized samples were saturated with 10% FBS in phosphate-buffered saline (PBS) (both from Sigma-Aldrich, USA) for 15 min and stained for vinculin using mouse monoclonal anti-vinculin antibody (V9264, Sigma Aldrich, USA) dissolved in 10% FBS in PBS for 30 min followed by Alexa Fluor 555 Goat anti-mouse IgG (BioLegend) as a secondary antibody (30 min). To simultaneously visualize actin, FITC–phalloidin (Invitrogen, Thermo Fisher Scientific, USA) was added to the secondary antibody solution at a final concentration of 1:100. Fluorescent images were acquired using a fluorescence microscope Thunder Imager Live Cell (Leica Microsystems, Heerbrugg, Switzerland) at 20× magnification.

2.14. Artificial Wound Healing (Scratch) Assay with Nanofiber Overlays

To assess cell migration within a 3D nanofibrillar context, we employed a previously established methodology described by Gugutkov et al. [34,37]. AD-MSCs were seeded in 12-well plates (Corning, Glendale, AZ, USA) and cultured in 1 mL DMEM/F12 supplemented with 10% FBS and 1% antibiotic–antimycotic solution (all from Sigma-Aldrich, USA). Once cultures reached approximately 90% confluence, a linear scratch was intro-

duced across the monolayer using a sterile 200 µL pipette tip. The SNFs were mounted on custom 3D-printed circular holders designed for this assay. Immediately after scratching, a nanofibrous mat (random or aligned) attached to the holder was gently positioned over the monolayer, ensuring direct contact between the dorsal cell surface and the overlying fibrous structure. This configuration enables evaluation of the so-called 'dorsal cell response,' as mechanical scratching cannot be performed directly on the nanofibrous mat without compromising its architecture. Indeed, this overlay approach represents the only feasible and reproducible method for studying directed migration on electrospun fibers. Cells monolayers without nanofibers were used as controls. The samples were further incubated in DMEM/F12 with 1% antibiotic-antimycotic solution and 10% fetal serum (FBS) and observed using the live cell chamber of the inverted fluorescent microscope (Thunder Imager Live Cell, Leica Microsystems, Switzerland) in time-lapse mode (every 15 min at 10× magnification) for 24 h. The closure of the scratched area was quantified using ImageJ software version 1.54p (Wayne Rasband, National Institute of Mental Health, NIH, Bethesda, MD, USA) with a plug-in for high-throughput image analysis particularly designed for in vitro scratch assays [38]. The percentage of wound closure was calculated as

$$\% \text{ Closure} = [(A_0 - A_t)/A_0] \times 100,$$

where A_0 is the wound area at 0 h and A_t is the area at time t.

2.15. Statistical Analysis

Statistical analyses were performed using GraphPad Prism 8 (GraphPad Software, Boston, MA, USA). Data are presented as column bar graphs, scatter plots with individual points representing independent replicates, line graphs, or percentage stacked bar charts. Normality was assessed using the Shapiro–Wilk test, followed by evaluation of variance homogeneity with Bartlett's test. The assumption of sphericity was evaluated using Mauchly's test. The statistical tests applied, the corresponding significance levels, and the number of replicates is reported in the respective figure legends.

3. Results

3.1. Characterization of Hybrid Secretome-PLCL Nanofibers

To fulfill the main goal of this study, we embedded secretome derived from Wharton's Jelly mesenchymal stem cells (WJ-MSCs) into electrospun poly(L-lactide-co-ε-caprolactone) (PLCL) nanofibers. Our previous research [38] demonstrated that this secretome notably and significantly affects the proliferation and migration of MSCs from other sources. The integration followed a modified version of the established protocol for producing hybrid fibrinogen/PLCL nanofibers, originally developed at the Institute for Bioengineering of Catalonia (IBEC), Barcelona, Spain. PLCL and lyophilized secretome were separately dissolved in hexafluoroisopropanol (HFIP) and mixed in a 1:1 ratio, resulting in final concentrations of 60 mg/mL for PLCL and 0.15 mg/mL for the secretome The resulting solutions corresponded to polymer concentrations of 6% (*w*/*v*) for secretome-functionalized nanofibers (SNFs) and 12% (*w*/*v*) for control PLCL nanofibers. Randomly oriented and aligned nanofibers were produced via direct electrospinning onto a grounded electrode or a rotating drum collector, respectively, as outlined in the Methods section.

As shown on Figure 2A,B, control PLCL nanofibers (CNFs) exhibited uniform morphology across both random (R-CNFs) and aligned (A-CNFs) configurations. Incorporation of the WJ-MSC secretome (SNFs), however, resulted in a significant reduction in average fiber diameter, discernible even under low-magnification (20×) phase-contrast images

(Figure 2G,H). More precise size determination was performed by AFM, as shown below in Section 3.1.5.

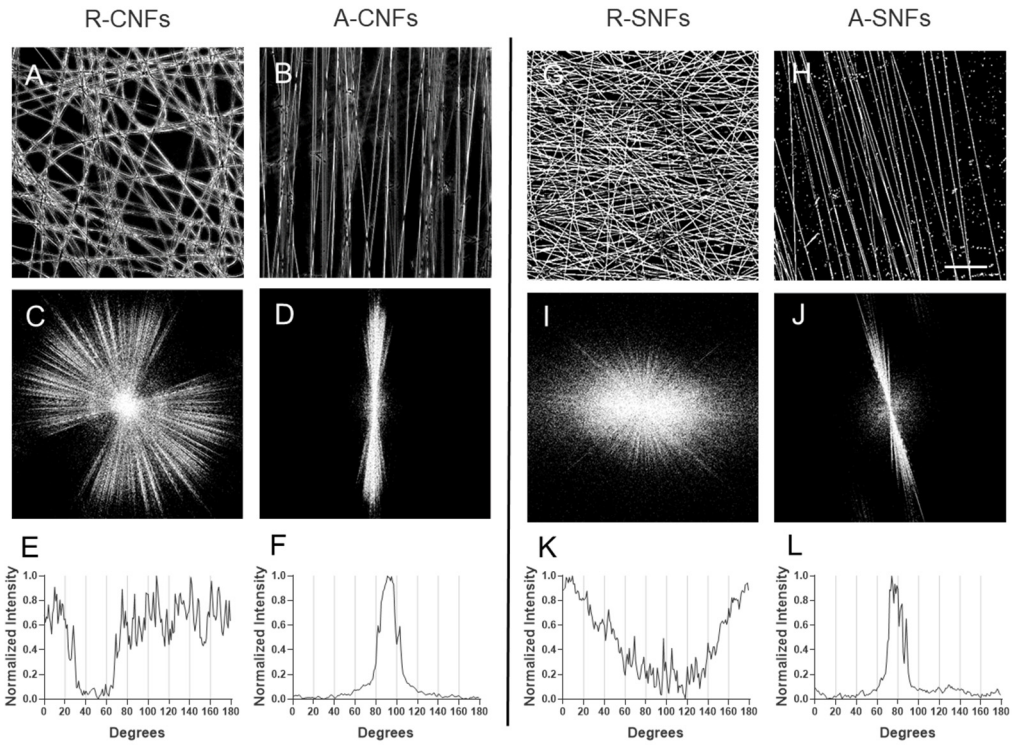

Figure 2. Overall morphology and Fast Fourier Transform (FFT) analysis of nanofiber alignment. Phase-contrast images (**A**,**B**) of control random R-CNF (**A**) and aligned A-CNF (**B**) orientations versus hybrid random R-SNF (**G**) and aligned A-SNF (**H**) configurations, respectively. Corresponding FFT images for the control nanofibers (CNFs) with random R-CNF (**C**) and aligned A-CNF (**D**) configurations versus hybrid NFs with random R-SNFs (**I**) and aligned A-SNFs (**J**). The bottom row presents radial intensity profiles showing the degree of alignment for R-CNFs (**E**) and A-CNFs (**F**) versus hybrid SNFs in random R-SNF (**K**) and aligned A-SNF (**L**) configurations. Scale bar on (**A**,**B**,**G**,**H**): 20 μm.

3.1.1. Fast Fourier Transform (FFT) Analysis

FFT analysis was conducted to evaluate the alignment of nanofibers. Radial intensity profiles were extracted from the FFT patterns to assess fiber orientation (Figure 2C–J). Aligned nanofibers exhibited strongly anisotropic features in the frequency domain, with most of the intensity confined within an angular range of approximately 20°, observed for both control (CNFs; Figure 2D,F) and secretome-loaded nanofibers (SNFs; Figure 2J,L). In contrast, randomly oriented nanofibers displayed isotropic FFT patterns lacking any dominant angular distribution, consistent with the random morphology of control CNFs (Figure 2C,E) and secretome-loaded SNFs (Figure 2I,K).

3.1.2. Release Kinetics of Secretome from Nanofibers

To confirm the successful incorporation of the secretome into the PLCL nanofiber matrix, FITC-labeled secretome was used to fabricate hybrid nanofibers in both random and aligned configurations. Fluorescence imaging reveals a distinct fluorescence signal within nanofibers, confirming the presence of secretome-associated biomolecules (Figure 3A,B). Though some microscopic clusters might be observed on these samples, suggesting some irregular distribution of the incorporated secretome, the fluorescent signal generally followed the morphological pattern of the fibers in both random or aligned configuration.

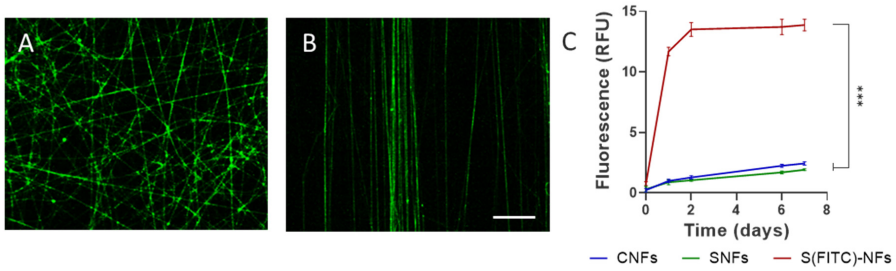

Figure 3. Distribution and release profile of FITC-labeled secretome from hybrid nanofibers (NFs). Fluorescence microscopy images of randomly oriented (**A**) and aligned (**B**) nanofibers incorporating FITC-labeled secretome illustrating its distribution. Panel (**C**) shows the quantitative release profile of FITC fluorescence, expressed in Relative Fluorescence Units (RFUs), from control PLCL nanofibers (CNFs), secretome-loaded nanofibers (SNFs) without FITC labeling, and FITC-labeled secretome-loaded nanofibers (S(FITC)NFs) in the supernatant (PBS) over time (days). Data are presented as mean ± standard deviation (SD) ($n = 4$). Statistical significance was assessed using repeated-measures ANOVA; Greenhouse–Geisser correction for potential sphericity violations was applied, followed by Tukey's multiple comparisons test, with *** indicating $p \leq 0.01$. Scale bars in (**A**,**B**): 20 µm.

The fluorescence assay further revealed a sustained release of fluorescently labeled secretome products from the SNFs for up to 48 h, followed by a plateau corresponding to a diffusion equilibrium with the surrounding medium (Figure 3C). Control PLCL nanofibers without incorporated secretome exhibited negligible florescence. Notably, because fluorescence intensity is not an intrinsic property and labeling efficiency cannot be determined, the data reflect relative release kinetics only.

3.1.3. Fourier Transformed Infrared Spectroscopy (FTIR) Analysis of the Nanofibers' Chemical Composition

While fluorescent imaging demonstrates the successful secretome incorporation into the nanofibers, FTIR analysis was employed to assess whether incorporation of the WJ-MSC secretome induces detectable changes in their chemical composition.

As shown in Figure 4, the IR spectra of neat PLCL (CNFs) and secretome-treated PLCL (SNFs) are nearly identical across the full spectral range. Both samples display the characteristic absorption bands of PLCL, including the ester carbonyl (C=O) stretching vibration at 1720–1735 cm^{-1} and the C–O–C stretching vibrations in the 1180–1080 cm^{-1} region [39]. However, despite the overall similarity, subtle spectral variations were detected in the 1700–1500 cm^{-1} region—differences may arise from the weak amide I/II vibrations of the low-abundance secretome proteins incorporated in the nanofiber structure [40].

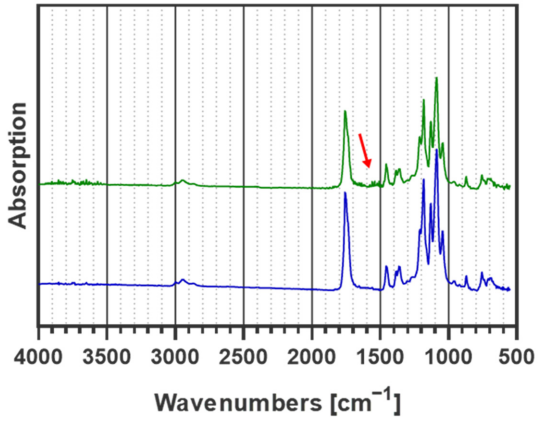

Figure 4. FTIR spectra of control plain PLCL (CNFs, blue) and secretome-loaded PLCL (SNFs, green). The arrow indicates the weak amide I/II vibration peak in SNFs, consistent with the presence of low-abundance secretome proteins.

3.1.4. Scanning Electron Microscopy (SEM)-Based Quantification of Fiber Diameter and Distribution

SEM analysis of fiber diameter revealed a pronounced reduction in nanofiber size following secretome incorporation. The average SEM- derived diameter of control CNFs was 1267 ± 95 nm, whereas SNFs exhibited a significantly smaller mean diameter of 575 ± 68 nm, corresponding to an approximately 2.2-fold decrease in fiber diameter (Figure 5). Nevertheless, the corresponding histograms display a normal (Gaussian) distribution in both nanofiber types (Figure 5B,D).

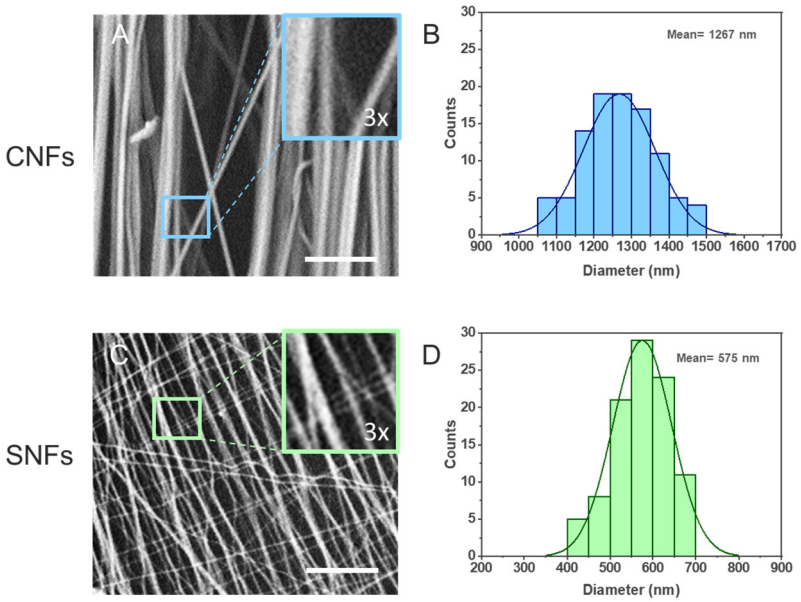

Figure 5. SEM images and nanofiber diameter distribution. (**A**) Representative SEM images of control nanofibers (CNFs) and (**B**) the corresponding diameter distribution. (**C**) Representative SEM images of secretome-functionalized nanofibers (SNFs) with (**D**) the corresponding diameter distribution. On A and C, insets with 3× magnification are provided. Scale bars: 30 µm.

3.1.5. Atomic Force Microscopy (AFM) Analysis of Nanofiber Morphology and Mechanical Properties

While SEM provided statistically robust information on nanofiber diameter distributions over large surface areas, AFM analysis was further employed to resolve nanoscale topographical features and cross-sectional geometry that cannot be fully captured by SEM.

Figure 6 shows representative 2D topographical AFM images of control nanofibers (Figure 6A–D) and secretome-functionalized nanofibers (Figure 6E–H). Both CNFs and SNFs formed continuous, well-defined fibrous networks with no signs of fiber fragmentation or loss of structural continuity following the incorporation of WJ-MSC secretome (Figure 6A,E).

AFM-derived geometrical parameters further demonstrate the morphological differences between the two fiber types (Table 1). Importantly, CNFs are 2888 ± 888.4 nm in height and 3882 ± 356.2 nm in width, resulting in a relatively low aspect ratio (1.45 ± 0.57). In contrast, SNFs have a much smaller height (121 ± 42.54 nm) and width (812 ± 176.1 nm), yielding a substantially higher aspect ratio (6.48 ± 0.82). This reduction correlates with the lower polymer concentration used during electrospinning (6% (*w*/*v*) for SNFs vs. 12% (*w*/*v*) for control plane PLCL NFs).

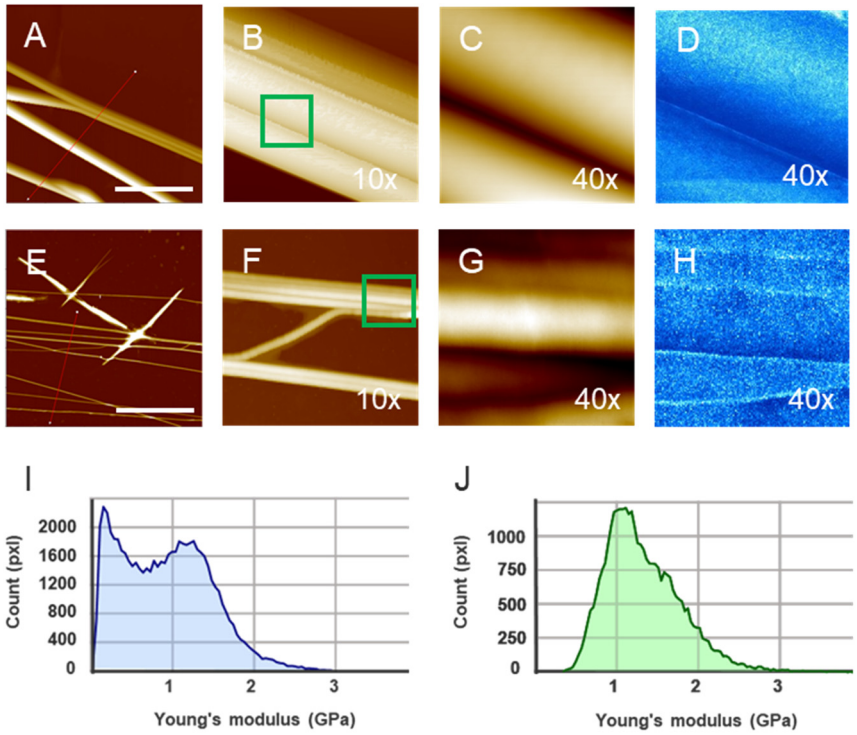

Figure 6. Atomic Force Microscopy (AFM) characterization of nanofibers. Representative AFM images of control nanofibers (CNFs; panels (**A**–**D**)) and secretome-functionalized nanofibers (SNFs; panels (**E**–**H**)). Panels (**A**,**E**) show topographical scans; (**B**,**F**) display 10× cross-sectional profiles; (**C**,**G**) present 40× cross-sectional profiles; (**D**,**H**) provide Young's modulus values scan of (**C**,**D**) cross-sectional fields. (**I**,**J**) present the histograms of Young's modulus values distribution for CNFs (**I**) and SNFs (**J**), respectively. Scale bars in (**A**,**E**): 20 µm.

Table 1. Summary of the quantitates of Young's modulus and cross-sectional area, derived from AFM images, presented as mean ± SD (n = 5). Statistical significance was assessed using unpaired T-test indicated as $p \leq 0.01$ (**) and $p \leq 0.001$ (***).

	Young's Modulus (GPa)	Size Hight (nm)	Size Width (nm)	Cross-Sectional Area (µm^2)	Aspect Ratio
CNFs	0.99 ± 0.18	2888 ± 888.4	3882 ± 356.2	8.73 ± 2.53	1.45 ± 0.57
SNFs	1.49 ± 0.22	121 ± 42.54	812 ± 176.1	0.08 ± 0.04	6.48 ± 0.82
***p*-value**	**	***	***	***	**

Thus, both SEM and AFM consistently demonstrate the same trend, i.e., secretome incorporation results in significantly thinner nanofibers formation, though the local fibers superposition at certain crossing points, captured in the AFM line profiles, may contribute to an overestimation of lateral dimensions.

On the other hand, the Young's modulus histogram of CNFs revealed a broad distribution of the values, with two partially overlapping populations (Figure 6I), indicating pronounced mechanical heterogeneity across the analyzed areas (Figure 6D). Thus, the average modulus of CNFs is 0.99 ± 0.18 GPa, with substantial variability (Table 1). In contrast, SNFs exhibit a single, well-defined population of Young's modulus values (Figure 6J), indicating a mechanically more homogeneous system. Compared to CNFs, the distribution is narrower, reflecting reduced variability in the mechanical response (Figure 6H). The mean Young's modulus of SNFs is 1.49 ± 0.22 GPa (Table 1), which is markedly higher than that of CNFs. These results coincide with the differences in the geometry of the nanofibers. Presumably, the markedly reduced height and higher aspect ratio of SNFs promote stronger

mechanical coupling between the fibers and the underlying rigid substrate during AFM nanoindentation. As a result, substrate constraint contributes more uniformly to the measured response, leading to higher apparent modulus values and a narrower distribution compared to the thicker and more irregular CNFs.

3.2. Cellular Interaction

3.2.1. Overall Morphology and Spreading of AD-MSCs Adhering to Secretome-Containing Nanofibers

AD-MSCs did not initially attach well to the non-loaded PLCL nanofibers under short term incubation (5 h), remaining rounded and poorly spread, which prevented quantitative analysis of cell morphology and spreading on these scaffolds. However, this observation underscores the critical role of the incorporated WJ-MSC secretome in promoting initial cell adhesion and cytoskeletal organization.

As shown on Figure 7, immunofluorescence staining conducted five hours post-incubation demonstrated effective cell attachment on both random and aligned SNFs, with distinct morphological patterns. AD-MSC exhibited a rather stellate shape on random nanofibers (Figure 7A,B) and more of a spindle-like morphology on aligned nanofibers (Figure 7C,D). The presence of vinculin-positive clusters (Figure 7B,D) at the cell periphery marked with arrows indicates the formation of strong focal adhesions, while the pronounced actin stress fibers across both substrates suggest efficient cell spreading and well-organized cytoskeletal architecture. These findings confirm that secretome-functionalized nanofibers support stem cell adhesion. Additionally, the emergence of elongated cell morphology on aligned nanofibers further implies that MSCs actively sense and respond to the nanofiber orientation.

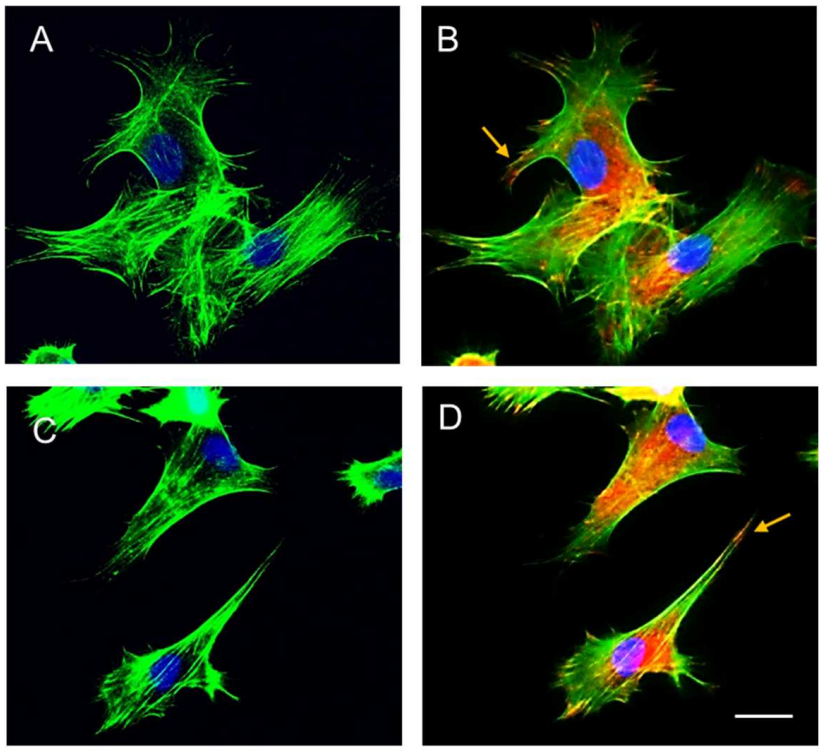

Figure 7. Immunostaining of vinculin clusters and actin filaments in MSCs cultivated for 5 h on (**A**,**B**) random and (**C**,**D**) aligned secretome nanofibers (SNFs). Panels (**A**,**C**) show contrast-enhanced images highlighting the actin cytoskeleton (green), while panels (**B**,**D**) display the same fields with the additional visualization of vinculin (red). Yellow arrows indicate vinculin clusters. Nuclei are shown in blue in all images. Scale bar: 20 μm.

3.2.2. Morphometry Analysis of Cell Spreading and Elongation

Considering the heterogeneity in cell morphology, CellProfiler software version 4.2.8 was further employed to analyze the difference in the main cell spreading area of individually measured cells (Figure 8A,B).

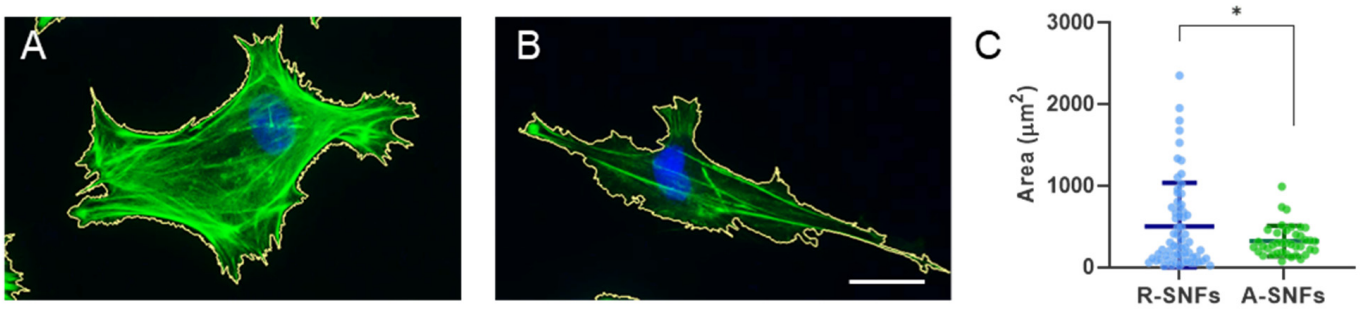

Figure 8. Cell morphology analysis of AD-MSCs cultured for 5 h on SNFs. Fluorescence images are showing cells cultured on (**A**) random and (**B**) aligned SNFs with actin filaments (green), cell nuclei (blue) and cell border overlays (yellow). (**C**) Quantitative morphometric analysis of the cell spreading area (in μm^2). is presented as mean ± SD (n = 40). Statistical significance was assessed using Kolmogorov–Smirnov test. Asterix denotes statistical significance of $p \leq 0.05$ (*). Scale bar: 20 µm.

Quantitative analysis demonstrated that the average cell spreading area was significantly greater ($p < 0.05$) on randomly oriented SNFs, revealing an area of approximately 500 μm^2, compared to 320 μm^2 on aligned fibers (Figure 8C). This finding suggests that the random fiber configuration offers multidirectional attachment sites, allowing cells to spread in various directions. Conversely, the aligned nanofibers seem to restrict the spreading area, encouraging an elongated morphology following the fibers' axis.

3.3. Stem Cell Culture on Secretome PLCL Nanofibers

To better understand how stem cells interact with hybrid SNFs over time, we ran a longer 3-day experiment. This study aimed to confirm that the secretome-containing nanofibers are biocompatible and biologically active during extended culture—an essential aspect of tissue regeneration.

3.3.1. Aligned Nanofibers Sustain AD-MSC Viability During Extended Culture

Cell viability is a fundamental parameter influencing subsequent cellular behavior. To assess the impact of secretome functionalization (SNFs) and fiber orientation, AD-MSC viability on SNFs was monitored at 24, 48, and 72 h (Figure 9A). Plain glass substrates (Figure 9A left panel) served as a positive control for cell survival. During the first 48 h, most cells were stained green with Calcein AM, and no major differences in viability were observed across conditions (apoptotic cells appear in red), although cultures on randomly oriented SNFs (middle panel) exhibited slightly reduced viability when multiple images (n = 4) were analyzed. By day 3, AD-MSCs cultured on aligned SNFs (A-SNFs) maintained high viability throughout the entire culture period, comparable to the glass control, whereas cells on randomly oriented SNFs (R-SNFs) showed a marked increase in apoptotic cells (Figure 9A, middle panel), confirmed by quantification across samples (Figure 9B). These results indicate that nanofiber alignment plays a distinct role in supporting AD-MSC vitality during prolonged culture.

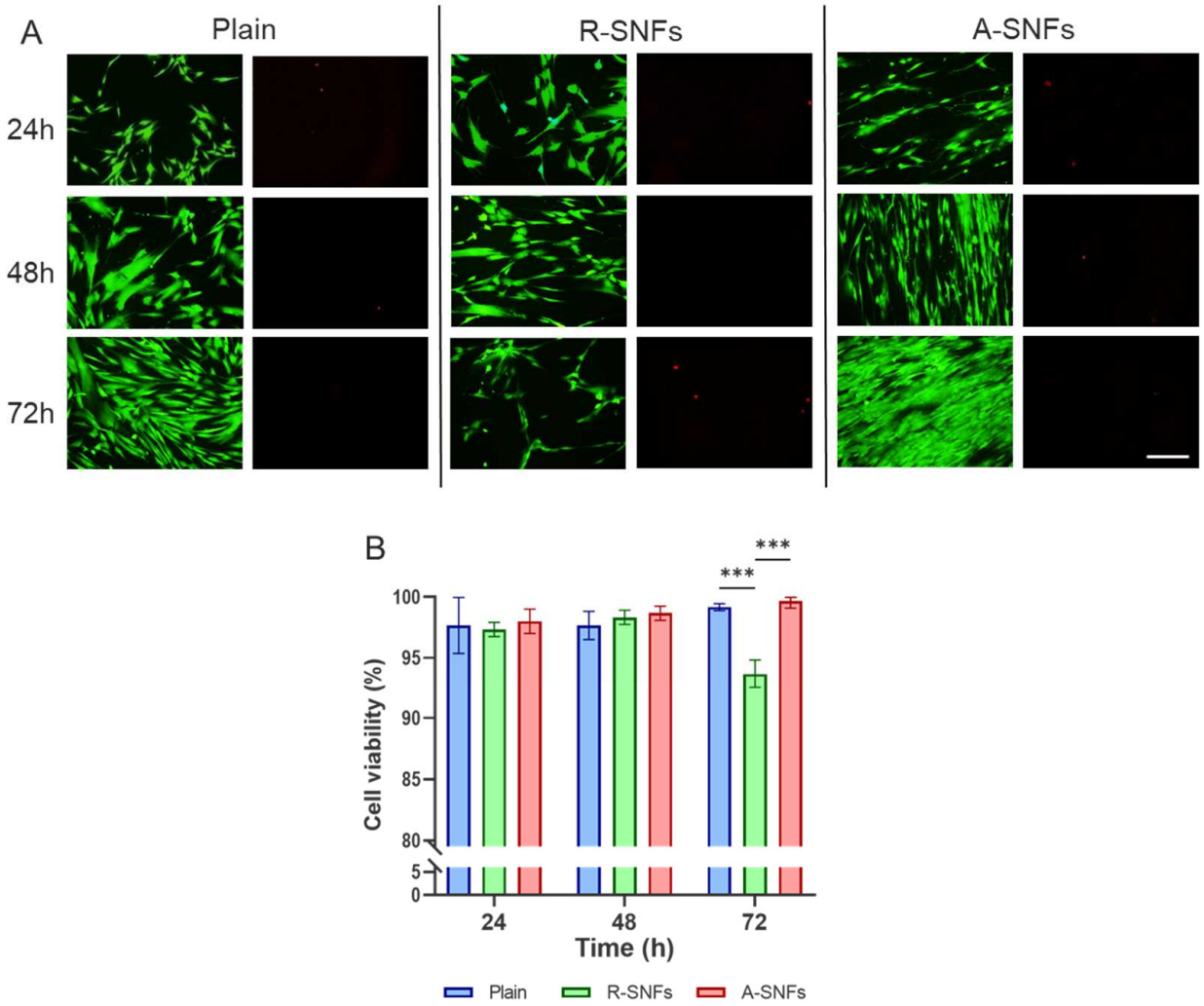

Figure 9. Aligned nanofibers maintain AD-MSC viability during extended culture. (**A**) Representative fluorescence micrographs of AD-MSCs cultured on plain glass (control), random secretome nanofibers (R-SNFs), and aligned ones (A-SNFs) for 72 h. Live cells are stained with Calcein AM (green) and dead cells with propidium iodide (red). (**B**) Quantitative analysis of cell viability (%) at 24, 48, and 72 h. Data are presented as mean ± SD (n = 4). Error bars above 100% were truncated at the upper bound of the scale. Statistical analysis was performed using two-way ANOVA, followed by Tukey's multiple comparisons test. Asterisks denotes statistical significance of $p \leq 0.001$ (***). Scale bar on panel (**A**) = 50 μm.

3.3.2. FFT Analysis of Cell Orientation

After 24 h of culture, cells on A-SNFs displayed a pronounced unidirectional alignment, resulting in elongated morphologies (Figure 10A(g)). This contrasted with the disordered cellular arrangement observed on R-SNFs and control glass substrates (Figure 10A(d) and Figure 10A(a), respectively). Interestingly, stem cells on R-SNFs tended to cluster (Figure 10A(d)), suggesting a propensity for homotypic interactions. Fast Fourier Transform (FFT) analysis supported these findings, revealing a distinct anisotropic frequency domain for cells on A-SNFs (Figure 10A(h)), in contrast to the more isotropic patterns seen on control and R-SNF surfaces (Figure 10A(b,e)). The radial intensity profile for A-SNFs was concentrated within an angular range of approximately 60° (Figure 10A(i)), indicating strong cellular alignment along the nanofiber orientation. In comparison, cells on R-SNFs and the control substrate exhibited diffuse, isotropic FFT profiles lacking directional preference (Figure 10A(c,f)).

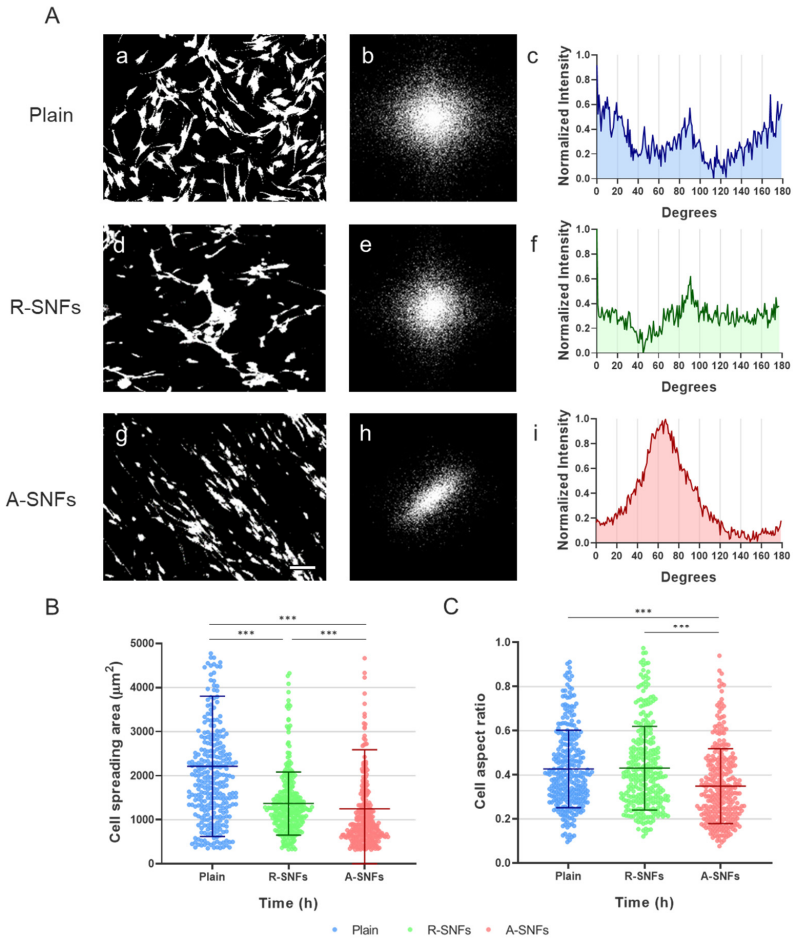

Figure 10. Aligned nanofibers guide directional orientation and promote elongated morphology in AD-MSCs at 24 h of incubation. (**A**) Fast Fourier Transform (FFT) analysis of AD-MSC orientation. Representative high-contrast fluorescent images of calcein-stained cells and corresponding analyses are shown for control glass substrates (a–c), randomly oriented secretome nanofibers (R-SNFs; d–f), and aligned secretome nanofibers (A-SNFs; g–i). Panels a, d, and g display cell morphology; panels b, e, and h show the corresponding FFT images; and panels c, f, and i present radial intensity profiles. (**B**) Quantification of cell spreading area (CSA) at 24 h of culture. (**C**) Quantification of cell aspect ratio (AR) for the same cell populations. Data are presented as mean ± SD (n = 300). Statistical significance was assessed using the Kruskal–Wallis test and Dunn's multiple comparisons test. Asterisks denotes statistical significance of $p \leq 0.001$ (***). Scale bar for panels (**A**) a, d, and g is 50 µm.

Further quantitative morphometric analysis at 24 h of incubation (Figure 10B,C) revealed a significant decrease in cell spreading area (CSA) and a corresponding increase in aspect ratio (AR) for AD-MSCs cultured on A-SNFs, indicating a more elongated cell morphology compared to both R-SNFs and control substrates. Notably, cells on R-SNFs also exhibited a moderate reduction in CSA relative to the control (plain glass substrate), though this effect was less pronounced than that observed with aligned nanofibers.

3.3.3. Nanofiber Alignment Supports AD-MSC Proliferation

Quantitative analysis of AD-MSC proliferation at 24, 48, and 72 h (Figure 11) revealed a significant increase in cell density on aligned nanofibers (A-SNFs), particularly evident at the 72 h mark (Figure 11A). This was accompanied by a notable reduction in cell doubling time (Figure 11B), estimated to be approximately fourfold shorter than on R-SNFs and about half that of the control glass substrate, suggesting an enhanced proliferation rate. In contrast, cells cultured on randomly oriented nanofibers (R-SNFs) exhibited markedly

slower proliferation, with an estimated doubling time of around 130 h—substantially longer than the approximate 70 h for the control glass substrates and 25 h for A-SNFs.

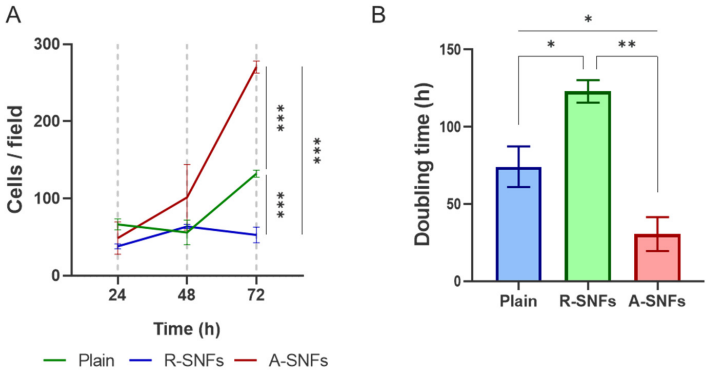

Figure 11. Aligned nanofibers promote stem cell proliferation compared to random nanofibers configurations (**A**) Proliferation dynamics of AD-MSCs on control plain glass and the secretome PLCL nanofibers (SNFs) over 24, 48, and 72 h, presented as the number of cells per field. (**B**) Cell doubling time over the 72 h culture period. Data are presented as mean ± SD (n = 4). Statistical significance was assessed using one-way ANOVA, followed by Tukey's multiple comparisons test. Asterisks denotes statistical significance of $p \leq 0.05$ (*), $p \leq 0.01$ (**), and $p \leq 0.001$ (***). For graph (**A**), it was the analysis was performed at the final time point (72 h).

3.3.4. The Nanofiber Configuration Modulates Cell Cycle Progression of AD-MSC

To assess in more details whether nanofiber architecture influences the proliferation dynamics of AD-MSCs, cell cycle distribution was evaluated after 48 h of culture on plain substrates, randomly oriented SNFs (R-SNFs), and aligned SNFs (A-SNFs) using image-based fluorometric analysis of individual cells (Figure 12). Cells cultured on plain glass and R-SNFs exhibited similar profiles, with a dominant population in the G1 and S phases and a smaller fraction in G2/M (Figure 12A,B). In contrast, AD-MSCs grown on A-SNFs (Figure 12C) showed a pronounced shift in cell cycle dynamics, marked by a decreased proportion of cells in G1 and an approximately fivefold increase in the G2/M population compared to the control (Figure 12D). Additionally, the S phase fraction was reduced nearly fourfold relative to both the control and R-SNFs, indicating accelerated progression through DNA synthesis and entry into mitosis. These results suggest that an aligned nanofiber configuration enhances proliferative activity by promoting G1 phase exit and facilitating cell cycle progression.

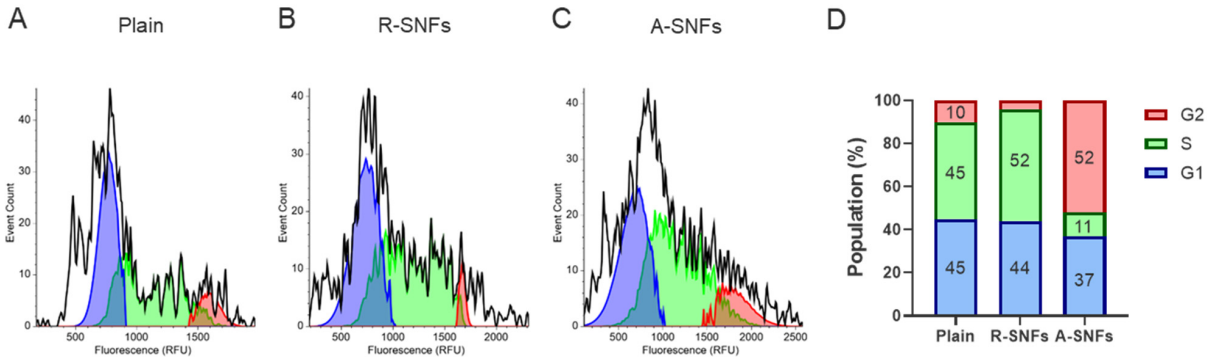

Figure 12. Aligned SNFs modulate cell cycle phase distribution of AD-MSCs after 48 h of culture. (**A**–**C**) Representative histograms illustrating cell cycle profiles of AD-MSCs cultured for 48 h on (**A**) plain glass substrate, (**B**) randomly oriented secretome-functionalized PLCL nanofibers (R-SNFs), and (**C**) aligned nanofibers (A-SNFs). Data are shown as event count versus fluorescence intensity. (**D**) Quantitative summary of the percentage of cells in G1, S, and G2/M phases under each condition.

3.3.5. Spheroids Formation

As shown above, AD-MSCs cultured on randomly oriented secretome-functionalized nanofibers (R-SNFs) exhibited reduced viability and slower proliferation compared to those grown on aligned nanofibers (A-SNFs) and control surfaces, particularly evident at the 72 h time point (Figures 9 and 11 above). Continued incubation up to six days in a follow-up experiment confirmed this trend, as live/dead staining consistently revealed a lower proportion of viable cells on R-SNFs—a pattern already evident on day 3 in previous experiments (Figure 9B). Since the fibers were electrospun using the same method and duration, and potential cytotoxicity differences can likely be excluded, this prompted a closer examination of cell morphology during the extended 6-day culture period.

By day 1, cells on R-SNFs began forming visible clusters (Figure 13A(a,d)), which progressed into early spheroid structures by day 3 (Figure 13A(b,e)), culminating in mature spheroids by day 6 (Figure 13A(c,f)). These 3D aggregates were frequently associated with increased cell death, particularly in their cores by day 3. By day 6, mature spheroids displayed pronounced central apoptosis, likely due to restricted nutrient and oxygen diffusion within the dense structures (Figure 13B).

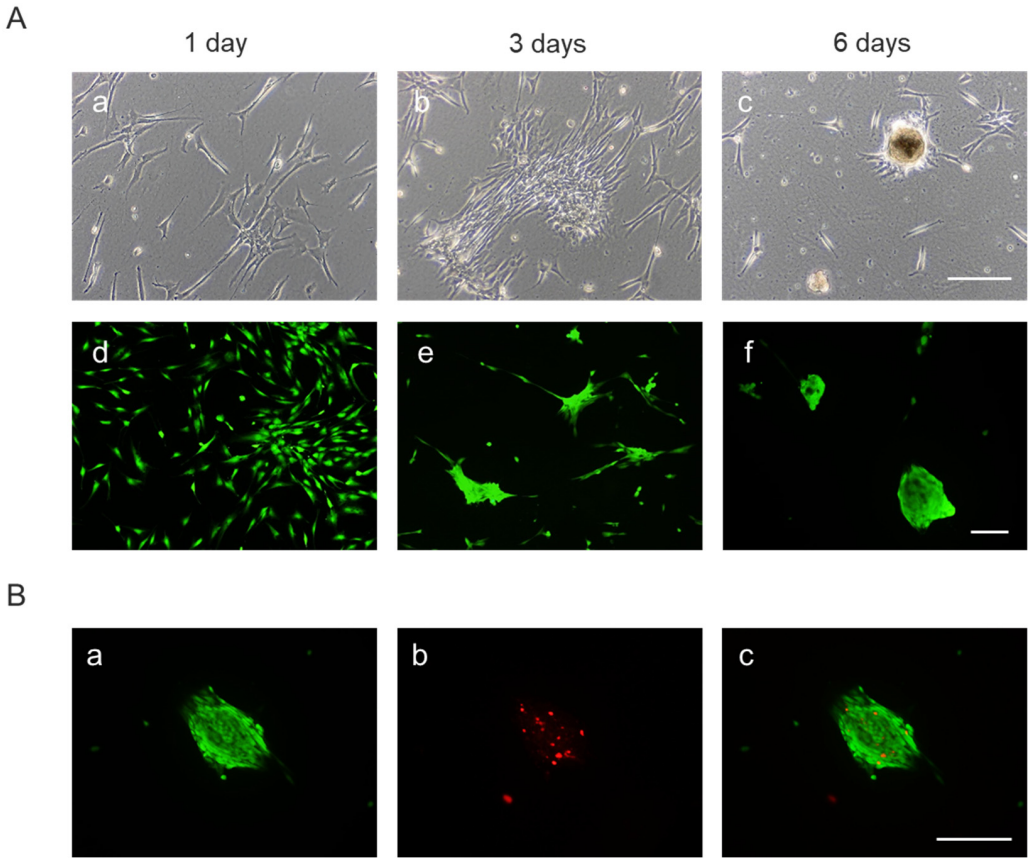

Figure 13. Random nanofibers induce spheroid formation. (**A**) Phase-contrast (a–c) and fluorescence (d–f) images of spheroids formed after 6 days cultivation of AD-MSCs on SNFs (live cells in green). (**B**) Live/dead assay of the spheroids (a–c) at day 6 (viable cells in green, non-viable cells in red). Scale bars = 100 μm.

These observations suggest that while random nanofiber substrates facilitate spheroid formation, they may also create micro environmental limitations that compromise long-term cell survival.

3.4. In Vitro Wound Healing Assay

As shown in Figure 14, in vitro wound healing (scratch) assays with AD-MSCs demonstrated that aligned secretome-functionalized PLCL nanofibers (A-SNFs) significantly enhanced cell migration (Figure 14A) and accelerated wound closure (Figure 14B, C) compared to control substrates. In contrast, randomly oriented nanofibers resulted in slower cell movement and delayed wound area closure.

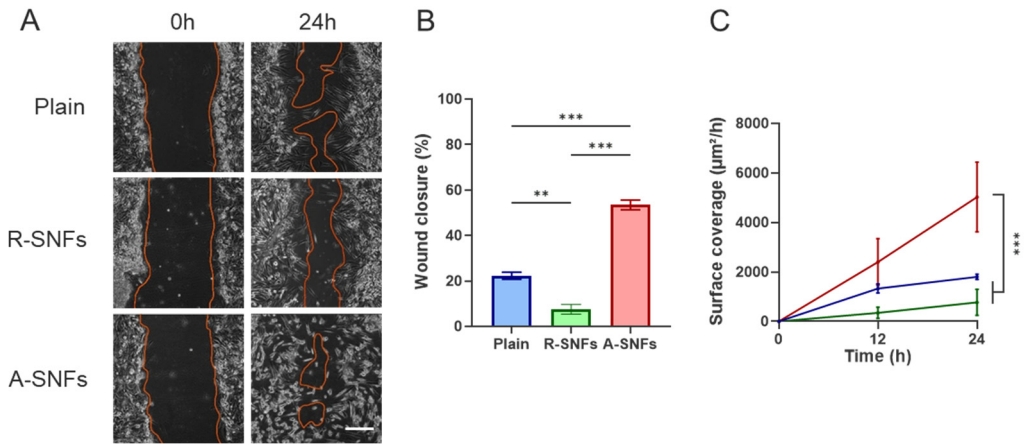

Figure 14. Aligned secretome PLCL nanofibers promote AD-MSC migration, while random fibers inhibit it. (**A**) Phase-contrast images of AD-MSCs at 0 h (**left**) and 24 h (**right**). The initial wound area is marked by an orange line, which also delineates the closed region at the endpoint. (**B**) Graph showing the percentage of wound closure after 24 h. (**C**) Quantitative analysis of the surface coverage over time. Data are color-coded: control with no nanofibers (blue), as well as cell monolayers with random SNFs (green) and with aligned SNFs (red). Statistical significance was assessed using one-way ANOVA, followed by Tukey's multiple comparisons test (for the 24 h mark in (**C**)). Asterisks denotes statistical significance of $p < 0.05$ (**) and $p < 0.001$ (***). Scale bar: 100 µm.

These findings further underscore the importance of fiber alignment in providing directional cues that support coordinated cell migration and promote efficient wound healing.

4. Discussion

This study provides a comprehensive biological and biophysical characterization of hybrid poly(L-lactide-co-ε-caprolactone) (PLCL) nanofibers functionalized with secretome derived from Wharton's Jelly mesenchymal stem cells (WJ-MSCs). The use of AD-MSCs for biological assays models the response of resident stromal cells to exogenously delivered secretome-loaded nanofibers (SNFs), a scenario highly relevant for regenerative medicine. By integrating the structural versatility of electrospun PLCL with the regenerative bioactivity of stem-cell-derived secretome, our aim was to develop a multifunctional scaffold capable of directing cell behavior and enhancing tissue repair.

Electrospinning of PLCL under optimized conditions produced nanofibers with uniform morphology in both random and aligned configurations. Incorporation of the WJ-MSC secretome resulted in a pronounced reduction in fiber diameter, visible even at low magnification and confirmed by SEM and AFM analyses. SEM revealed an approximately twofold decrease in diameter, from 1267 ± 95 nm in control CNFs to 575 ± 68 nm in SNFs. AFM measurements corroborated this reduction in the size of fibers and additionally indicated a higher aspect ratio in SNFs, suggesting partial fiber flattening. A question arises: ***why did fiber morphology change following secretome addition***? Given the difference in polymer concentration—12% for CNFs versus 6% for SNFsthe narrower diameter distribution in SNFs can be partly attributed to the lower solution viscosity, which, under the controlled

electrospinning conditions used here, may promote greater jet elongation and contribute to finer fiber formation [18,34].

Notably, both CNFs and SNFs retained Gaussian diameter distributions, indicating uniform and reproducible fiber formation despite the presence of bioactive components. The apparent flattening observed in SNFs by AFM may reflect altered solvent evaporation dynamics, with thinner fibers drying more rapidly than the thicker CNFs.

Fast Fourier Transform (FFT) analysis further demonstrated that aligned nanofibers exhibited strong anisotropy, with intensity confined to a narrow angular range (~20°), whereas randomly oriented fibers displayed isotropic patterns. These findings confirm that our methodology provides robust control over fiber orientation, a key parameter for directing cell alignment and functional behavior [41]. AFM measurements unexpectedly showed a higher apparent Young's modulus for SNFs compared with control fibers. Although stiffness can positively influence cell–material interactions, this increase is unlikely to be biologically relevant, as SNFs were produced from a lower PLCL concentration. The most plausible explanation is geometric: the smaller diameter and higher aspect ratio of SNFs increase their effective contact with the rigid glass substrate during indentation, artificially elevating the measured modulus.

Collectively, these geometric changes not only alter the mechanical behavior of the fibers but also increase the available surface area and introduce topographical cues that can facilitate cell attachment and enhance the bioactive performance of a putative scaffold. This naturally raises the next important question of ***whether secretome incorporation improves cell adhesion to PLCL fibers***.

Our findings indicate that it does: Secretome-containing nanofibers markedly enhance AD-MSC interaction, likely through integrin-mediated mechanisms, as evidenced by the formation of well-developed focal adhesions and a robust actin cytoskeleton. In contrast, the control plain PLCL fibers (CNFs) fail to support comparable attachment, underscoring the functional contribution of secretome-derived adhesive cues.

Fluorescence imaging of FITC-labeled secretome confirmed its successful incorporation into the nanofiber matrix, although some heterogeneity in distribution was evident. FTIR analysis further indicated that secretome addition did not alter the chemical integrity of the PLCL backbone, as no major peak shifts were detected. However, in secretome-containing samples, subtle amide I/II signals in the 1700–1500 cm^{-1} region were repeatedly observed. Although their intensity is comparable to the spectral noise level, their consistent appearance suggests the presence of trace amounts of secretome-derived proteins associated with the fiber surface. Even at such a low abundance, adhesive components—like fibronectin, vitronectin, or laminin fragments—can modulate surface properties and promote cell attachment. Moreover, this interpretation aligns with our biological observations, where AD-MSCs exhibited markedly improved interaction with secretome-containing fibers (SNFs), indicating that these surface-associated protein traces contribute functionally to the enhanced cellular response.

Biologically, the smaller submicron fibers may also contribute for the successful cellular interaction, as more closely mimic the size of native extracellular matrix components, such as collagen and elastin fibers, providing increased surface area for cell attachment and improved presentation of bioactive cues [42]. Such nanoscale topography has been shown to influence cytoskeletal organization, focal adhesion formation, and mechanotransduction pathways, ultimately promoting alignment, proliferation, and directional migration of mesenchymal stem cells [43]. Therefore, secretome incorporation not only introduces biochemical functionality but also beneficially modulates scaffold architecture, reinforcing the hybrid nanofibers' potential for regenerative applications.

4.1. Insights to Cell Adhesion, Morphology, and Spreading

Immunofluorescence staining at 5 h post-seeding showed that AD-MSCs adhered effectively to both random and aligned SNFs adopting a stellate-like morphology or spindle-like shapes, respectively, with prominent actin stress fibers and vinculin-positive focal adhesions. These observations indicate robust cytoskeletal organization and suggest that nanofiber orientation influences cell morphology and adhesion dynamics [44]. Quantitative analysis of cell spreading area revealed that AD-MSCs on random SNFs exhibited significantly larger spreading areas (~500 μm^2) compared to those on aligned SNFs (~320 μm^2). This suggests that random fibers provide multidirectional anchoring points, while aligned fibers constrain spreading and promote elongation along the fiber axis [45].

These morphological findings can be attributed to the distinct topographical cues provided by the nanofiber architecture. Aligned nanofibers present anisotropic guidance signals that promote cell elongation and orientation along the fiber axis, a well-established contact guidance phenomenon [46,47]. In contrast, randomly oriented fibers create an isotropic surface that supports more heterogeneous spreading and reduced directional organization. Importantly, as noted in the Results section, the inability of cells to adhere to non-loaded control nanofibers (CNFs) further underscores the critical role of the incorporated secretome in providing essential biochemical cues that complement the physical guidance of the scaffold. The MSC secretome is rich in a variety of adhesion-promoting components, including fibronectin, laminin, vitronectin, and matricellular proteins [27]. When incorporated into otherwise weakly adhesive polymers such as PLCL, these bioactive molecules supply integrin-binding ligands that enable cells to recognize the substrate. This promotes focal adhesion formation and supports stable cell attachment and spreading, facilitating effective cell–material interactions and downstream functional responses [48].

4.2. Cell Alignment, Viability, and Proliferation

After 24 h of culture, FFT analysis of cell orientation confirmed that AD-MSCs on aligned SNFs displayed strong unidirectional alignment, with radial intensity profiles concentrated within ~60°, in contrast to the disordered patterns on random SNFs and control substrates.

Viability assays over 72 h demonstrated that aligned SNFs supported sustained AD-MSC vitality, while random SNFs showed increased apoptosis by day 3. This trend persisted through day 6, with live/dead staining revealing mature spheroid formation on random SNFs accompanied by central apoptosis—likely due to limited nutrient and oxygen diffusion within dense 3D aggregates. These findings align with prior reports on diffusion limitations in spheroid cultures [49].

Aligned SNFs significantly enhanced also AD-MSC proliferation, as demonstrated by increased cell counts and shortened doubling times over a 72 h culture period. Cell cycle analysis revealed a marked shift toward the G2/M phase in cells grown on aligned SNFs, with a fivefold increase compared to control substrates, accompanied by a notable reduction in the S phase population. These findings suggest that aligned nanofibers promote proliferative activity by facilitating exit from the G1 phase and accelerating progression through the cell cycle. This observation aligns with the results reported by Amores de Sousa et al. [50], who showed that functionalization and alignment of electrospun nanofibers enhanced neural stem cell proliferation and increased the proportion of cells in both the S and G2/M phases, indicative of accelerated mitotic entry.

All these effects might be attributed to the release secretome-associated multiple growth factors, including bFGF, VEGF, EGF, HGF, etc., which are known to activate the MAPK/ERK and PI3K/Akt signaling pathways, thereby enhancing cell proliferation and survival [26]. These bioactive cues are likely the main contributors to the reduced doubling

time observed on aligned secretome-functionalized nanofibers (A-SNFs). However, their effect possibly acts in concert with the geometric cues provided by the fiber organization. This is evident in the ability of aligned SNFs to promote MSC proliferation and survival, where the anisotropic topography supports cell elongation and sustained cytoskeletal tension. Such morphology is typically associated with enhanced activation of mechanotransduction pathways, including focal adhesion kinase (FAK) and YAP/TAZ signaling. FAK activation reinforces focal adhesion maturation and cytoskeletal organization, while nuclear YAP/TAZ drives transcriptional programs linked to cell cycle progression, survival, and immunomodulatory activity in ASCs [51]. Together, this coordinated mechanotransduction creates a permissive microenvironment for AD-MSC expansion and functional activation. In contrast, this pro-proliferative and profunctional response is not observed on R-SNFs, where isotropic topography disrupts cytoskeletal tension and dampens FAK and YAP/TAZ activity, allowing unfavorable architectural cues to override biochemical stimulation.

While the combination of fiber alignment and secretome incorporation appeared to enhance cellular responses, a formal statistical interaction analysis was not performed; thus, these effects are described as complementary rather than definitively synergistic, and such an analysis will be pursued in future studies.

4.3. In Vitro Wound Healing and Migration

In vitro scratch assays demonstrated that aligned SNFs significantly enhanced AD-MSC migration and accelerated wound closure compared to random SNFs and control substrates. These results highlight the critical role of fiber alignment in providing directional cues that promote coordinated cell movement—an essential feature for effective tissue regeneration [52,53].

These findings are consistent with previous reports showing that mechanical stretching and cell elongation activate FAK and the Piezo1/F-actin/YAP signaling pathway more effectively, thereby promoting enhanced MSC migration and proliferation [51,54].

5. Conclusions

Overall, our findings demonstrate that the biological activity of secretome-functionalized PLCL nanofibers emerges from the combined contribution of biochemical cues and fiber geometry. Secretome-derived adhesive proteins provide an initial molecular interface for MSC attachment, while the anisotropic architecture of aligned SNFs reinforces cytoskeletal tension and promotes sustained activation of mechanotransduction pathways such as FAK and YAP/TAZ. This coordinated biochemical–biophysical signaling environment supports robust AD-MSC proliferation, survival, and functional activation. In contrast, randomly oriented SNFs fail to provide the necessary topographical guidance, leading to diminished cytoskeletal organization and attenuated mechanotransductive signaling despite the presence of the same biochemical factors. These results underscore the importance of integrating both biochemical composition and structural design when engineering bioactive scaffolds for regenerative applications.

Author Contributions: Conceptualization, G.A.; methodology G.A. and D.G.; methodology, cell culture, writing, and software analysis, T.S. and L.T. with equal contribution; data curation, T.S. and L.T.; writing—original draft preparation, writing, G.A.; editing, G.A. and S.T.; supervision, G.A.; resources, S.K. and I.B.-T.; funding acquisition, G.A., R.K.-P., S.T. and D.D. All authors have read and agreed to the published version of the manuscript.

Funding: This research was funded by the European Union NextGenerationEU through the National Recovery and Resilience Plan of the Republic of Bulgaria, project BG RRP 2.004 0003, with additional support by the Medical University–Pleven, Bulgaria (internal MU project 13/2026), specifically for electrospinning of secretome loaded nanofibers, FTIR characterization, and time lapse microscopy

analyses. The authors also acknowledge the financial support of project BG16RFPR002 1.014 0002 C001, "Center of Competence in Personalized Medicine, 3D and Telemedicine, Robotic Assisted and Minimally Invasive Surgery," funded by PRIDST 2021–2027 and co funded by the European Union, particularly for the cell culture processing, immunofluorescence measurements and related quantitative analyses.

Institutional Review Board Statement: This study was conducted according to the guidelines of the Declaration of Helsinki and approved by the Institutional Ethics Committee of Medical University—Pleven (approval 745-KENID, approval date 5 June 2023).

Data Availability Statement: The original contributions presented in this study are included in the article. Further inquiries can be directed at the corresponding author.

Acknowledgments: We acknowledge support through Leonardo da Vinci Center of Competence in Personalized Medicine, 3D and Telemedicine, Robotic and Minimally Invasive Surgery, Pleven, Bulgaria.

Conflicts of Interest: The authors declare no conflicts of interest.

Abbreviations

The following abbreviations are used in this manuscript:

PLCL	Poly(L-lactide-co-ε-caprolactone)
WJ-MSCs	Wharton's jelly-derived mesenchymal stem cells
FTIR	Fourier Transform Infrared Spectroscopy
SEM	Scanning Electron Microscopy
AFM	Atomic Force Microscopy
FFT	Fast Fourier Transform
AD-MSCs	Adipose-Derived MSCs
ECM	Extracellular Matrix
PLA	Poly(Lactic Acid)
FDA	Food and Drug Administration
MSCs	Mesenchymal Stem Cells
VEGF	Vascular Endothelial Growth Factor
bFGF	Basic Fibroblast Growth Factor
EGF	Epidermal Growth Factor
TGF-β	Transforming Growth Factor-β
mRNA	Messenger RNA
HFIP	Hexafluoroisopropanol
R-NFs	Random Nanofibers
A-NFs	Aligned Nanofibers
CNFs	Control Nanofibers
SNFs	Secretome Nanofibers
NCM	Non-Contact Mode
FITC	Fluorescein Isothiocyanate
GPC	Gel Permeation Chromatography
PBS	Phosphate-Buffered Saline
FBS	Fetal Bovine Serum

References

1. Boateng, J.S.; Matthews, K.H.; Stevens, H.N.E.; Eccleston, G.M. Wound Healing Dressings and Drug Delivery Systems: A Review. *J. Pharm. Sci.* **2008**, *97*, 2892–2923. [CrossRef] [PubMed]
2. Guo, S.; DiPietro, L.A. Factors Affecting Wound Healing. *J. Dent. Res.* **2010**, *89*, 219–229. [CrossRef] [PubMed]
3. Chouhan, D.; Mandal, B.B. Silk Biomaterials in Wound Healing and Skin Regeneration Therapeutics: From Bench to Bedside. *Acta Biomater.* **2020**, *103*, 24–51. [CrossRef]

4. Ye, K.; Kuang, H.; You, Z.; Morsi, Y.; Mo, X. Electrospun Nanofibers for Tissue Engineering with Drug Loading and Release. *Pharmaceutics* **2019**, *11*, 182. [CrossRef]
5. Xue, J.; Wu, T.; Dai, Y.; Xia, Y. Electrospinning and Electrospun Nanofibers: Methods, Materials, and Applications. *Chem. Rev.* **2019**, *119*, 5298–5415. [CrossRef]
6. Fuloria, S.; Subramaniyan, V.; Dahiya, R.; Dahiya, S.; Sudhakar, K.; Kumari, U.; Sathasivam, K.; Meenakshi, D.U.; Wu, Y.S.; Sekar, M.; et al. Mesenchymal Stem Cell-Derived Extracellular Vesicles: Regenerative Potential and Challenges. *Biology* **2021**, *10*, 172. [CrossRef]
7. Li, D.; Xia, Y. Electrospinning of Nanofibers: Reinventing the Wheel? *Adv. Mater.* **2004**, *16*, 1151–1170. [CrossRef]
8. Vizoso, F.J.; Eiro, N.; Cid, S.; Schneider, J.; Perez-Fernandez, R. Mesenchymal Stem Cell Secretome: Toward Cell-Free Therapeutic Strategies in Regenerative Medicine. *Int. J. Mol. Sci.* **2017**, *18*, 1852. [CrossRef]
9. Koh, C.T.; Low, C.Y.; Yusof, Y. Bin Structure-property Relationship of Bio-Inspired Fibrous Materials. *Procedia Comput. Sci.* **2015**, *76*, 411–416. [CrossRef]
10. Woodruff, M.A.; Hutmacher, D.W. The Return of a Forgotten Polymer—Polycaprolactone in the 21st Century. *Prog. Polym. Sci.* **2010**, *35*, 1217–1256. [CrossRef]
11. Zhang, M.; Chang, Z.; Wang, X.; Li, Q. Synthesis of Poly(l-lactide-co-ε-caprolactone) Copolymer: Structure, Toughness, and Elasticity. *Polymers* **2021**, *13*, 1270. [CrossRef]
12. Dhayer, M.; Barral, V.; Cleret, D.; Jordao, A.; Drucbert, A.-S.; Germain, N.; Dropsit, S.; Maboudou, P.; Dekiouk, S.; Brun, S.; et al. Material and Biological Characterization of 3D Knitted Bioresorbable Poly (D,L-lactide) (PLA) and Polycaprolactone (PCL) Scaffolds for Soft Tissue Regeneration: From Fabrication to In Vivo Performance. *J. Biol. Eng.* **2025**, *19*, 53. [CrossRef] [PubMed]
13. Eryildiz, M.; Karakus, A.; Eksi, M.A. Development and Characterization of PLA/PCL Blend Filaments and 3D Printed Scaffolds. *J. Mater. Eng. Perform.* **2025**, *34*, 14043–14054. [CrossRef]
14. Cipitria, A.; Skelton, A.; Dargaville, T.R.; Dalton, P.D.; Hutmacher, D.W. Design, Fabrication and Characterization of PCL Electrospun Scaffolds—A Review. *J. Mater. Chem.* **2011**, *21*, 9419–9453. [CrossRef]
15. Gentile, P.; Chiono, V.; Carmagnola, I.; Hatton, P.V. AnOverview of Poly(lactic-co-glycolic) acid (PLGA)-based Biomaterials for Bone Tissue Engineering. *Int. J. Mol. Sci.* **2014**, *15*, 3640–3659. [CrossRef]
16. Xie, J.; Li, X.; Xia, Y. Putting Electrospun Nanofibers to Work for Biomedical Research. *Macromol. Rapid Commun.* **2008**, *29*, 1775–1792. [CrossRef]
17. Liao, S.; Li, B.; Ma, Z.; Wei, H.; Chan, C.; Ramakrishna, S. Biomimetic Electrospun Nanofibers for Tissue Regeneration. *Biomed. Mater.* **2006**, *1*, R45–R53. [CrossRef]
18. Bhardwaj, N.; Kundu, S.C. Electrospinning: A fascinating Fiber Fabrication Technique. *Biotechnol. Adv.* **2010**, *28*, 325–347. [CrossRef]
19. Sill, T.J.; von Recum, H.A. Electrospinning: Applications in Drug Delivery and Tissue Engineering. *Biomaterials* **2008**, *29*, 1989–2006. [CrossRef]
20. Huang, Z.M.; Zhang, Y.Z.; Kotaki, M.; Ramakrishna, S. A Review on Polymer Nanofibers by Electrospinning and their Applications in Nanocomposites. *Compos. Sci. Technol.* **2003**, *63*, 2223–2253. [CrossRef]
21. Badami, A.S.; Kreke, M.R.; Thompson, M.S.; Riffle, J.S.; Goldstein, A.S. Effect of Fiber Diameter on Spreading, Proliferation, and Differentiation of Osteoblastic Cells on Electrospun Poly(lactic acid) Substrates. *Biomaterials* **2006**, *27*, 596–606. [CrossRef]
22. Li, W.-J.; Laurencin, C.T.; Caterson, E.J.; Tuan, R.S.; Ko, F.K. Electrospun Nanofibrous Structure: A Novel Scaffold for Tissue Engineering. *J. Biomed. Mater. Res.* **2002**, *60*, 613–621. [CrossRef]
23. Abbasian, S.; Shafaei, N.; Daraeinejad, Z.; Rajabi, M.; Shabani, I. Investigating the Effect of Alignment on Electrospun Nanofiber Properties and Regulating Cellular Behaviors. *Polym. Rev.* **2025**, *66*, 109–158. [CrossRef]
24. Margiana, R.; Markov, A.; Zekiy, A.O.; Hamza, M.U.; Al-Dabbagh, K.A.; Al-Zubaidi, S.H.; Hameed, N.M.; Ahmad, I.; Sivaraman, R.; Kzar, H.H.; et al. Clinical Application of Mesenchymal Stem Cell in Regenerative Medicine: A Narrative Review. *Stem Cell Res. Ther.* **2022**, *13*, 336. [CrossRef] [PubMed]
25. Zhang, B.; Tian, X.; Hao, J.; Xu, G.; Zhang, W. Mesenchymal Stem Cell-Derived Extracellular Vesicles in Tissue Regeneration. *Cell Transplant.* **2020**, *29*. [CrossRef] [PubMed]
26. Prado-Yupanqui, J.W.; Ramírez-Orrego, L.; Cortez, D.; Vera-Ponce, V.J.; Chenet, S.M.; Tejedo, J.R.; Tapia-Limonchi, R. The Hidden Power of the Secretome: Therapeutic Potential on Wound Healing and Cell-Free Regenerative Medicine—A Systematic Review. *Int. J. Mol. Sci.* **2025**, *26*, 1926. [CrossRef]
27. Novoseletskaya, E.; Grigorieva, O.; Nimiritsky, P.; Basalova, N.; Eremichev, R.; Milovskaya, I.; Kulebyakin, K.; Maria, K.; Rodionov, S.; Omelyanenko, N.; et al. Mesenchymal Stromal Cell-Produced Components of Extracellular Matrix Potentiate Multipotent Stem Cell Response to Differentiation Stimuli. *Front. Cell Dev. Biol.* **2020**, *8*, 555378. [CrossRef]
28. Krasnodembskaya, A.; Song, Y.; Fang, X.; Gupta, N.; Serikov, V.; Lee, J.-W.; Matthay, M.A. Antibacterial Effect of Human Mesenchymal Stem Cells Is Mediated in Part from Secretion of the Antimicrobial Peptide LL-37. *Stem Cells* **2010**, *28*, 2229–2238. [CrossRef]

29. Alcayaga-Miranda, F.; Cuenca, J.; Khoury, M. Antimicrobial Activity of Mesenchymal Stem Cells: Current Status and New Perspectives of Antimicrobial Peptide-Based Therapies. *Front. Immunol.* **2017**, *8*, 339. [CrossRef]
30. Liu, X.; Yang, Y.; Li, Y.; Niu, X.; Zhao, B.; Wang, Y.; Bao, C.; Xie, Z.; Lin, Q.; Zhu, L. Integration of Stem Cell-Derived Exosomes with In Situ Hydrogel Glue as a Promising Tissue Patch for Articular Cartilage Regeneration. *Nanoscale* **2017**, *9*, 4430–4438. [CrossRef]
31. Zhang, J.; Liu, X.; Li, H.; Chen, C.; Hu, B.; Niu, X.; Li, Q.; Zhao, B.; Xie, Z.; Wang, Y. Exosomes/Tricalcium Phosphate Combination Scaffolds can Enhance Bone Regeneration by Activating the PI3K/Akt Signaling Pathway. *Stem Cell Res. Ther.* **2016**, *7*, 136. [CrossRef]
32. Phinney, D.G.; Pittenger, M.F. Concise Review: MSC-Derived Exosomes for Cell-Free Therapy. *Stem Cells* **2017**, *35*, 851–858. [CrossRef] [PubMed]
33. Stoyanova, T.; Topalova, L.; Kyurkchiev, S.; Komsa-Penkova, R.; Todinova, S.; Altankov, G. Selective Paracrine Modulation of Stromal Cells: Wharton's Jelly MSC Secretome Enhances Adipose-Derived MSC Functionality While Maintaining Dermal Fibroblast Quiescence. *Int. J. Mol. Sci.* **2025**, *26*, 10095. [CrossRef] [PubMed]
34. Gugutkov, D.; Gustavsson, J.; Cantini, M.; Salmeron-Sánchez, M.; Altankov, G. Electrospun Fibrinogen–PLA Nanofibres for Vascular Tissue Engineering. *J. Tissue Eng. Regen. Med.* **2017**, *11*, 2774–2784. [CrossRef] [PubMed]
35. O'Connell, B. Oval Profile Plot. Available online: https://imagej.net/ij/plugins/oval-profile.html (accessed on 20 September 2025).
36. Stirling, D.R.; Swain-Bowden, M.J.; Lucas, A.M.; Carpenter, A.E.; Cimini, B.A.; Goodman, A. CellProfiler 4: Improvements in Speed, Utility and Usability. *BMC Bioinform.* **2021**, *22*, 433. [CrossRef]
37. Gugutkov, D. Nanoengineering Approaches for Guiding Cellular Behavior. Ph.D. Thesis, Universitat Politècnica de Catalunya, Barcelona, Spain, 2017. [CrossRef]
38. Suarez-Arnedo, A.; Figueroa, F.T.; Clavijo, C.; Arbeláez, P.; Cruz, J.C.; Muñoz-Camargo, C. AnImage J Plugin for the High Throughput Image Analysis of In Vitro Scratch Wound Healing Assays. *PLoS ONE* **2020**, *15*, e0232565. [CrossRef]
39. de Souza, J.R.; Cardoso, L.M.; de Toledo, P.T.A.; Rahimnejad, M.; Kito, L.T.; Thim, G.P.; Campos, T.M.B.; Borges, A.L.S.; Bottino, M.C. Biodegradable Electrospun Poly(L-lactide-co-ε-caprolactone)/Polyethylene glycol/Bioactive Glass Composite Scaffold for Bone Tissue Engineering. *J. Biomed. Mater. Res. Part B Appl. Biomater.* **2024**, *112*, e35406. [CrossRef]
40. Barth, A. Infrared Spectroscopy of Proteins. *Biochim. Biophys. Acta-Bioenerg.* **2007**, *1767*, 1073–1101. [CrossRef]
41. Wang, S.; Zhong, S.; Lim, C.T.; Nie, H. Effects of Fiber Alignment on Stem Cells–Fibrous Scaffold Interactions. *J. Mater. Chem. B* **2015**, *3*, 3358–3366. [CrossRef]
42. Ushiki, T. The Three-Dimensional Ultrastructure of the Collagen Fibers, Reticular Fibers and Elastic Fibers: A Review. *Kaibogaku Zasshi.* **1992**, *67*, 186–199. Available online: https://europepmc.org/article/med/1523957 (accessed on 20 September 2025).
43. Yim, E.K.F.; Leong, K.W. Significance of Synthetic Nanostructures in Dictating Cellular Response. *Nanomed. Nanotechnol. Biol. Med.* **2005**, *1*, 10–21. [CrossRef]
44. Bashur, C.A.; Dahlgren, L.A.; Goldstein, A.S. Effect of Fiber Diameter and Orientation on Fibroblast Morphology and Proliferation on Electrospun Poly(D,L-lactic-co-glycolic acid) Meshes. *Biomaterials* **2006**, *27*, 5681–5688. [CrossRef] [PubMed]
45. Huang, C.-Y.; Hu, K.-H.; Wei, Z.-H. Comparison of Cell Behavior on PVA/PVA-Gelatin Electrospun Nanofibers with Random and Aligned Configuration. *Sci. Rep.* **2016**, *6*, 37960. [CrossRef] [PubMed]
46. Kai, D.; Prabhakaran, M.P.; Jin, G.; Ramakrishna, S. Guided Orientation of Cardiomyocytes on Electrospun Aligned Nanofibers for Cardiac Tissue Engineering. *J. Biomed. Mater. Res. Part B Appl. Biomater.* **2011**, *98*, 379–386. [CrossRef] [PubMed]
47. Yin, Z.; Chen, X.; Chen, J.L.; Shen, W.L.; Hieu Nguyen, T.M.; Gao, L.; Ouyang, H.W. The Regulation of Tendon Stem Cell Differentiation by the Alignment of Nanofibers. *Biomaterials* **2010**, *31*, 2163–2175. [CrossRef]
48. Dalby, M.J.; Gadegaard, N.; Oreffo, R.O.C. Harnessing Nanotopography and Integrin-Matrix Interactions to Influence Stem Cell Fate. *Nat. Mater.* **2014**, *13*, 558–569. [CrossRef]
49. Ryu, N.-E.; Lee, S.-H.; Park, H. Spheroid Culture System Methods and Applications for Mesenchymal Stem Cells. *Cells* **2019**, *8*, 1620. [CrossRef]
50. Amores de Sousa, M.C.; Rodrigues, C.A.V.; Ferreira, I.A.F.; Diogo, M.M.; Linhardt, R.J.; Cabral, J.M.S.; Ferreira, F.C. Functionalization of Electrospun Nanofibers and Fiber Alignment Enhance Neural Stem Cell Proliferation and Neuronal Differentiation. *Front. Bioeng. Biotechnol.* **2020**, *8*, 580135. [CrossRef]
51. Wan, S.; Fu, X.; Ji, Y.; Li, M.; Shi, X.; Wang, Y. FAK- and YAP/TAZ Dependent Mechanotransduction Pathways are Required for Enhanced Immunomodulatory Properties of Adipose-Derived mesenchymal stem Cells Induced by Aligned Fibrous Scaffolds. *Biomaterials* **2018**, *171*, 107–117. [CrossRef]
52. Gugutkov, D.; Gonzalez-Garcia, C.; Altankov, G.; Salmeron-Sánchez, M. Fibrinogen Organization at the Cell-Material Interface Directs Endothelial Cell Behavior. *J. Bioact. Compat. Polym.* **2011**, *26*, 375–387. [CrossRef]

53. Yang, F.; Murugan, R.; Wang, S.; Ramakrishna, S. Electrospinning of Nano/Micro Scale Poly(L-lactic acid) Aligned Fibers and their Potential in Neural Tissue Engineering. *Biomaterials* **2005**, *26*, 2603–2610. [CrossRef]
54. Ma, N.; Huang, L.; Zhou, Q.; Zhang, X.; Luo, Q.; Song, G. Mechanical Stretch Promotes the Migration of Mesenchymal Stem Cells via Piezo1/F-actin/YAP axis. *Exp. Cell Res.* **2025**, *446*, 114461. [CrossRef]